

ALMA MATER STUDIORUM · UNIVERSITÀ DI BOLOGNA

ENGINEERING SCHOOL

Master of Science in Aerospace Engineering

RANS-Based Aerodynamic Optimization of a Pickup Truck: Performance Assess- ment and Verification of Add-On Improve- ments

Supervisor:

Professor Guglielmo Minelli

Student:

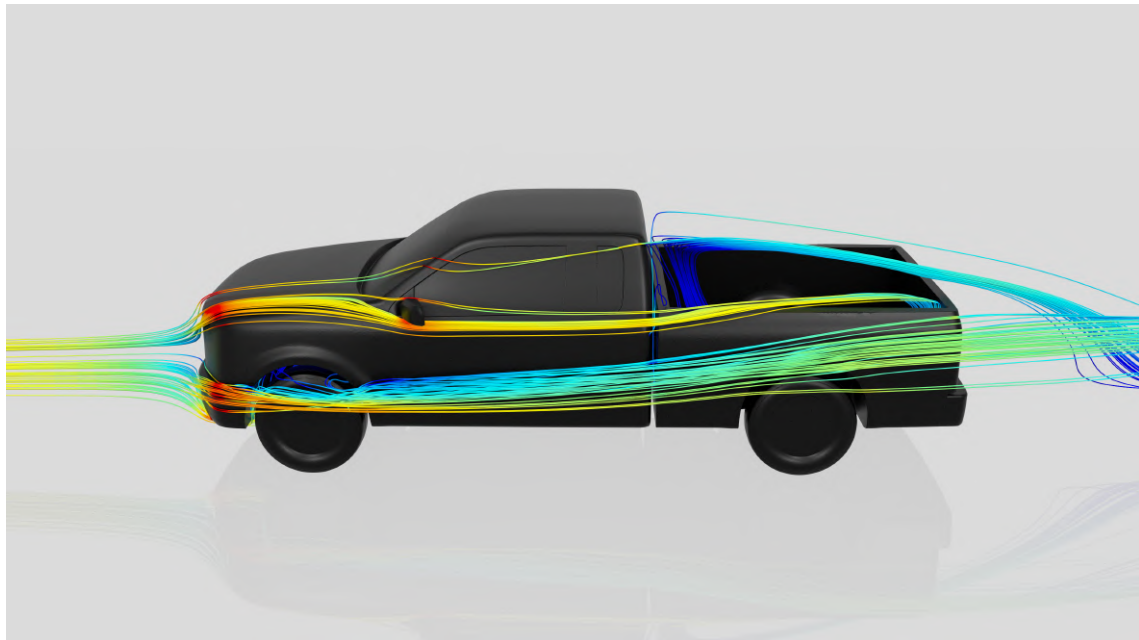
Alessandro Piferi

Academic Year 2024/2025

MASTER'S THESIS
ACADEMIC YEAR 2024/2025

RANS-Based Aerodynamic Optimization of a Pickup Truck: Performance Assessment and Verification of Add-On Improvements

ALESSANDRO PIFERI



Department of Industrial Engineering
Forlì Campus
UNIVERSITÀ DI BOLOGNA
Forlì, Italy, 10 December 2025

RANS-Based Aerodynamic Optimization of a Pickup Truck: Performance Assessment and Verification of Add-On Improvements

Alessandro Piferi

© Alessandro Piferi, 2025.

Supervisor: Professor Guglielmo Minelli, Department of Industrial Engineering

Master's Thesis 2024/2025
Department of Industrial Engineering
Università di Bologna



ALMA MATER STUDIORUM
UNIVERSITÀ DI BOLOGNA

Forlì, Italy, 10 December 2025

RANS-Based Aerodynamic Optimization of a Pickup Truck: Performance Assessment and Verification of Add-On Improvements

Alessandro Piferi
Department of Industrial Engineering
Università di Bologna

Abstract

Pickup trucks represent a significant share of the global automotive market yet remain characterized by poor aerodynamic efficiency due to their inherent bluff-body geometry. This study investigates the aerodynamics of a generic double-cab pickup truck, in two configurations: the open and closed bed, using steady state RANS turbulence model and wind tunnel validation. Three turbulence models, Realizable $k - \varepsilon$, Lag EB $k - \varepsilon$, and SST $k - \omega$ were evaluated against experimental data to determine the most accurate approach for predicting drag trends across configurations. The Lag EB $k - \varepsilon$ model demonstrated superior fidelity in predicting ΔC_D trends and was selected for the baseline flow topology study and optimization phases. The baseline flow topology analysis identified various critical sources of drag and the generation of a distinct pair of counter-rotating vortex that negatively impacts the drag generation. Several aerodynamic add-on devices were designed and assessed, including a sealed cabin-bed gap, a shortened tailgate, and a rear-cab spoiler. Results indicate that sealing the cabin-bed gap yields a drag reduction of approximately 2.0%. The optimal configuration, combining the gap seal with the spoiler, achieved a drag reduction of 3.2% for the open bed configuration and 2.4% for the closed bed configuration. These findings demonstrate that targeted management of the cabin wake and gap flow can significantly mitigate form drag without altering the primary vehicle architecture.

Keywords: Vehicle Aerodynamics, Pickup Truck, CFD, RANS, Turbulence Modeling, Drag Reduction, Wind Tunnel Testing, Wake Topology, Flow Control, Add-ons optimisation.

Acknowledgements

I would first like to acknowledge my supervisor, Professor Guglielmo Minelli, for his support, guidance, and encouragement throughout the entire thesis project. I am also deeply grateful to him for giving me the opportunity to conduct my work at Chalmers University of Technology.

My sincere thanks go to Simone Sebben and Alexey Vdovin for their exceptional availability, kindness, and support during my stay at Chalmers, and for allowing me to work within the Vehicle Engineering and Autonomous Systems division on this amazing project.

I would also like to thank Chao Xia, Tarun Kadri Sathiyan, and Avaneesh Upadhyaya for their valuable help, suggestions, and technical advices.

To my grandfather, who did not have the pleasure of seeing this. I am sure he would have said “boom boom boom.”

Alessandro Piferi, Forlì, 10 December 2025

List of Acronyms

Below is the list of acronyms that have been used throughout this thesis listed in alphabetical order:

BEV	Battery Electric Vehicle
CAD	Computer-Aided Design
CAGR	Compound Annual Growth Rate
CB	Closed Bed pickup model
CFD	Computational Fluid Dynamics
DDES	Delayed Detached Eddy Simulation
DES	Detached Eddy Simulation
DNS	Direct Numerical Simulation
DOF	Degrees of Freedom
ECARA	European Car Aerodynamics Research Association
EV	Electric Vehicle
GHG	Greenhouse Gas
GTU	Generic Truck Utility
ICE	Internal Combustion Engine
LES	Large Eddy Simulation
NEDC	New European Driving Cycle
OB	Open Bed pickup model
RANS	Reynolds Averaged Navier Stokes

RSS	Reynolds Stress Tensor
SUV	Sport Utility Vehicle
SST	Shear Stress Transport
URANS	Unsteady Reynolds Averaged Navier Stokes
WLTP	Worldwide Harmonised Light Vehicle Test Procedure

Nomenclature

Below is the nomenclature of parameters and variables that have been used throughout this thesis.

Symbol	Description	Unit
A	Frontal area	m^2
C_D	Drag coefficient	-
C_{DW}	Wind-averaged drag coefficient	-
C_L	Lift coefficient	-
C_P	Pressure coefficient	-
$C_{P_{tot}}$	Total pressure coefficient	-
F_D	Aerodynamic drag force	N
H	Vehicle overall height	m
k	Turbulent kinetic energy	m^2/s^2
L	Vehicle overall length	m
P_D	Power required to overcome drag	W
p	Static pressure	Pa
p_{tot}	Total pressure	Pa
Q	Q-criterion (vortex identification)	s^{-2}
Re	Reynolds number	-
S_{ij}	Mean strain rate tensor	s^{-1}
U, u	Velocity magnitude	m/s
u_i	Velocity component in i -direction	m/s
u'	Fluctuating velocity component	m/s

W	Vehicle overall width	m
y^+	Non-dimensional wall distance	-
β	Yaw angle	deg
ε	Turbulent dissipation rate	m^2/s^3
μ	Dynamic viscosity	$kg/(m \cdot s)$
μ_t	Turbulent eddy viscosity	$kg/(m \cdot s)$
ν	Kinematic viscosity	m^2/s
ν_t	Kinematic eddy viscosity	m^2/s
ω	Specific dissipation rate	s^{-1}
ρ	Air density	kg/m^3
τ_{ij}	Reynolds stress tensor	Pa

Contents

List of Acronyms	ix
Nomenclature	xii
List of Figures	xix
List of Tables	xxi
1 Introduction	1
1.1 Vehicle aerodynamics	1
1.2 Pickup Trucks and Aerodynamic Research	3
1.2.1 Drag Reduction Technologies	4
1.3 Thesis workflow	4
2 CFD theory	7
2.1 Reynolds Averaged Navier–Stokes	7
2.2 Turbulent models in Star-CCM+	10
2.2.1 Realizable $k - \varepsilon$	11
2.2.2 Lag EB $k - \varepsilon$	12
2.2.3 SST $k - \omega$	13
2.2.4 Models summary	15
3 Methodology	17
3.1 pickup truck model	17
3.2 CFD domain and setup	17
3.3 Mesh and convergence	19
3.4 Wind tunnel experiments	21
4 Results	27
4.1 Wind tunnel data	27
4.1.1 Comments on wind tunnel data	27
4.2 Turbulence models data	28
4.2.1 Comment on results	29
4.3 Aerodynamic analysis: closed versus open bed	30

Contents

4.4	Drag reduction aero-development	33
4.4.1	Closing the gap	38
4.4.2	Cutting the tailgate	38
4.4.3	Rear-cab spoiler	39
4.4.4	Optimal configuration	41
4.5	Best configuration analysis	42
5	Conclusions	49
	Bibliography	51

List of Figures

1.1	Thesis workflow.	5
3.1	The two baseline configurations studied.	18
3.2	Differences between ECARA GTU 3.2b 3.2d and baseline model 3.2a 3.2c.	18
3.3	Domain for half body car, L length, H height and W width of the pickup.	19
3.4	Workflow for mesh study.	21
3.5	Mesh sensitivity level study.	22
3.6	Selected mesh structure and details, with differences in prism layer structure between high y^+ and low y^+ treatment.	22
3.7	Histogram distribution of y^+ value normalized by body surface area. .	23
3.8	y^+ field distribution.	24
3.9	1:10 scaled pickup model mounted in the wind tunnel test section. .	25
3.10	Reynolds sweep test.	25
4.1	Drag coefficient for both OB and CB pickup baseline as function of β angle.	28
4.2	C_D value for each turbulence model, compared with wind tunnel value. .	29
4.3	ΔC_D between open bed and closed bed configurations for all turbu- lence models compared to wind tunnel prediction.	30
4.4	Velocity field and wake structure, closed and open bed baseline . . .	33
4.5	Pressure coefficient distribution on the front of the pickup baseline. .	34
4.6	Pressure coefficient distribution on the rear of the pickup baseline. .	34
4.7	Accumulated drag coefficient open bed and closed bed baseline. . .	35
4.8	Velocity field with convolution lines between the cabin-bed gap. . .	35
4.9	RC-Vortex behind the cabin, comparison open bed and closed bed baseline.	36
4.10	Isosurface for Q-criterion, $Q=1500$	36
4.11	Isosurface for Total Pressure Coefficient, $C_{P_{tot}} = 0$	37
4.12	Accumulated lift coefficient open bed and closed bed baseline. . . .	37
4.13	Side view of base line pickup with the cabin-bed gap closed. . . .	38
4.14	Tailgate modification.	39

List of Figures

4.15 Rear-cab spoiler front and back view.	39
4.16 Spoiler projection draw, measures in millimetres.	40
4.17 The two spoiler configurations.	40
4.18 Pressure coefficient distribution on the front and rear of the pickup baseline OB and best model OB.	44
4.19 Accumulated drag coefficient for best model both open and closed bed case.	45
4.20 Velocity field and wake structure, open bed baseline and best model OB.	45
4.21 Isosurface for Total Pressure Coefficient, $C_{P_{tot}} = 0$	46
4.22 Velocity and streamline projection on YZ plane for best model.	46
4.23 Isosurface for Q-criterion, Q=1500.	47
4.24 Streamlines behind the passenger cabin for best model.	48
4.25 Accumulated lift coefficient for best model both open and closed bed case.	48

List of Tables

2.1	Lag EB turbulent model coefficients	13
2.2	Comparative summary of the selected RANS turbulence models.	16
3.1	Baseline dimensions. See Figure 3.1 as reference.	17
3.2	Simulation settings.	19
3.3	Prism layer parameters.	21
3.4	Selected volume mesh parameters.	23
4.1	Fitting coefficients for wind averaged drag, Howell et al. [1].	27
4.2	Comparison between drag coefficient at $\beta = 0$ and C_{DW} value that estimate real wind conditions.	27
4.3	Design modification configuration identification code.	41
4.4	Effect of the introduced modifications.	41
4.5	Drag coefficient for best model OB and CB configurations, and Δ respect to relative baseline.	42
4.6	Lift coefficient for best model OB and CB configurations, Δ respect to relative baseline and relative vertical force generated with simulation conditions.	44

List of Tables

1

Introduction

1.1 Vehicle aerodynamics

This thesis is focused on pickup trucks, a specific passenger vehicle, aerodynamics analysis and optimization with verification and validation on simulation models.

Pickups combine personal transportation capacity of common SUV with the ability of carry loads, enabling people to travel and transport with personal goods, even in scenarios with rough and uneven paths and roads.

However, in the context of the European Green Deal and Global Greenhouse Gas (GHG) reduction targets, it is clear that fuel consumption and relative emissions need to be reduced. Passenger cars are a major polluter, accounting for 61% of total CO_2 emissions from EU road transport [2]. To achieve climate neutrality, the European Green Deal calls for a 90% reduction in greenhouse gas emissions from transport by 2050 [3].

Aerodynamics has become a critical lever for more energy efficient passenger vehicles. At low speeds the power train, rolling resistance and vehicle mass dominate the energy demand, but beyond roughly 80–100 km/h the aerodynamic drag becomes the largest single contribution to the road load [4]. Quantitative assessments in the literature show that, for a mid-size passenger car at 100 km/h, about 50–60% of the fuel consumption is associated with overcoming aerodynamic drag, and this fraction can exceed 65–70% for heavy-duty trucks at highway speed and legal gross weight [5]. Reducing drag therefore translates almost directly into lower fuel consumption or, for battery electric vehicles (BEVs), increased driving range.

The aerodynamic drag force acting on a vehicle with frontal area A travelling at speed U in air of density ρ is commonly written as

$$F_D = \frac{1}{2} \rho U^2 C_D A, \quad (1.1)$$

where C_D is the drag coefficient. The corresponding power required to overcome drag is $P_D = F_D U$, which scales with U^3 . At constant density and area, a 10% decrease in C_D leads to approximately a 10% reduction in drag force and drag

1. Introduction

power at a given speed. In practice, the industry targets reductions in the product $C_D A$ (the “drag area”), because both the coefficient and the frontal area can be adjusted through design.

Typical drag coefficients for current production vehicles are in the range $C_D \approx 0.25\text{--}0.30$ for streamlined sedans, $0.35\text{--}0.45$ for sport-utility vehicles, and $0.46\text{--}0.55$ for double-cab pickup trucks¹. These figures highlight the inherently bluff geometry of pickup vehicles and the challenge of achieving competitive aerodynamic performance [4–8].

The introduction of the Worldwide Harmonised Light Vehicle Test Procedure (WLTP) has further emphasized the importance of aerodynamics. Unlike the previous standard, the NEDC cycle², the WLTP features higher average speeds (46.5 km/h vs. 34 km/h for class 3 vehicles) and a higher maximum velocity, increasing the relative contribution of aerodynamic loads to the total energy consumption [9]. Therefore, even minor reductions in the drag coefficient (C_D) yield measurable benefits in fuel economy for Internal Combustion Engine (ICE) vehicles and range extension for Electric Vehicles (EVs).

The study of aerodynamic phenomena relies on three complementary pillars: wind tunnel testing, on-road coast-down tests, and Computational Fluid Dynamics (CFD). While wind tunnel testing remains the standard for validation, CFD has become indispensable for visualizing complex flow structures—such as the wake vortices behind a bluff body—that are difficult to capture experimentally [4].

The benefits of this combined approach are not limited to fuel or energy use. Improved aerodynamics also reduces sensitivity to crosswinds, enhances high-speed stability, lowers wind noise, improves cooling-air management and can reduce surface soiling of lamps, cameras and sensors [4, 5]. All of these aspects are important for modern vehicles with advanced driver-assistance systems and for future automated driving functions.

Road vehicles are bluff bodies operating close to the ground, with complex three-dimensional turbulent flows around the front end, underbody, wheels and rear.

The transition from ICE to electric powertrains has fundamentally altered the constraints of vehicle design. In electric vehicles, the energy density of batteries is significantly lower than that of liquid fuel, making energy efficiency, and thus drag reduction, paramount to alleviate “range anxiety”³ [6].

¹if we consider electric vehicles these numbers are at least 0.05 lower

²New European Driving Cycle

³Range anxiety is the driver’s fear that a vehicle has insufficient energy storage to cover the road distance needed to reach its intended destination [10]

This shift offers new aerodynamic opportunities. The removal of the bulky internal combustion engine and the associated driveshaft allows for a flatter underbody and reduced cooling requirements. Since electric motors operate at higher efficiencies with lower heat rejection than ICEs, the front cooling openings (grille) can be minimized or made active, reducing the internal drag caused by flow through the engine bay [4, 6]. Furthermore, the absence of a large engine block relaxes the packaging constraints on the front overhang. Recent studies suggest that optimizing the front overhang length and the curvature of the cabin roof can significantly delay flow separation, a design freedom less available in traditional truck architectures [6].

1.2 Pickup Trucks and Aerodynamic Research

The global pickup truck market size was valued at USD 219.94 billion in 2024 and is projected to grow from USD 231.81 billion in 2025 to reach USD 353.07 billion by 2033, growing at a CAGR⁴ of 5.4% during the forecast period (2025-2033) [11]. Despite the sales and market dominance of pickup trucks, particularly in North America and increasingly in global markets, their aerodynamic literature is sparse compared to passenger sedans and SUVs. Over the past two decades, the scientific community has produced a disproportionate number of studies on the aerodynamics of sport-utility vehicles (SUVs) compared to pickup trucks, a keyword search in Scopus [12] (May 2025) returns around 78 peer-reviewed articles containing the terms “SUV”, “aerodynamics”, “CFD” or “wind tunnel”, while an equivalent search for “pickup truck”⁵ yields less than 20 articles, with a ratio of around 4:1.

The pickup truck is aerodynamically characterized as a bluff body with a unique feature: a large, open cargo bed behind the passenger cabin. In addition, a pickup is characterised by a larger front section, ground clearance and footprint than the average non-commercial vehicle. All of those factors lead to high values of the C_D and the drag force.

The objective of this thesis is to investigate drag-reduction strategies for a simplified pickup truck. The approach is based on a structured methodology consisting of:

- validation of the simulation model against wind-tunnel data;
- analysis of the baseline aerodynamics;
- evaluation of geometric modifications aimed at reducing drag.

⁴Compound Annual Growth Rate

⁵pick AND up AND (aerodynamic OR drag OR aerodynamics OR CFD OR wind OR tunnel OR LES OR DDES OR RANS)

1.2.1 Drag Reduction Technologies

Aerodynamic research on pickups has focused extensively on the flow interaction between the cabin wake and the cargo bed. A persistent misconception is that lowering or removing the tailgate reduces drag. However, classical wind-tunnel experiments by Cooper [13] demonstrated that a closed tailgate generates a stable recirculating vortex inside the bed. This vortex forms a “virtual sloping surface” that guides the external flow over the bed and promotes a clean separation at the tailgate edge. Removing the tailgate destroys this structure, allowing the flow to impinge on the cab rear wall and increasing pressure drag [13]. Similarly, replacing the solid tailgate with a mesh net has been shown to increase drag significantly due to the flow losses through the mesh [13].

Effective drag reduction strategies documented in the literature include:

- **Tonneau Covers:** Covering the bed flush with the beltline prevents flow from entering the bed, essentially converting the vehicle into a sedan-like shape. This can yield drag reductions of up to 10% [13].
- **Cab Roof Spoilers:** Extensions at the rear of the cab which modify the shear-layer trajectory and mitigate flow re-attachment on the tailgate [6].
- **Geometric Modifications:** Recent optimization studies suggest that tapering the cab roof and adjusting the front overhang length can postpone the stagnation point and separation lines, yielding significant drag improvements [6].

Despite these advances, there remains a gap in the literature regarding the detailed optimization of add-on devices for specific flow regimes, such as the interaction between cab spoilers and the specific vortex structures generated by the A-pillars and the cab-bed gap. Furthermore, while SUV wake topology is well-documented [14], the specific sensitivity of the pickup truck’s unique wake structure to minor geometric changes in the cab-to-bed transition region requires further investigation.

1.3 Thesis workflow

The thesis is organised into three phases. First, several RANS turbulence models are assessed and validated against wind-tunnel measurements. Second, the baseline configuration is analysed to characterize the primary flow structures. Third, targeted add-on modifications are designed and evaluated with the aim of reducing drag.

A schematic representation of this workflow is shown in Figure 1.1.

1. Study, verification and validation, of turbulence models. In this phase, various simulation models are compared with wind tunnel reference values;
2. Baseline analysis and validation. Aerodynamic characterization of the baseline model;

3. Drag reduction study with add-on design.

The thesis workflow is illustrated in Figure 1.1.

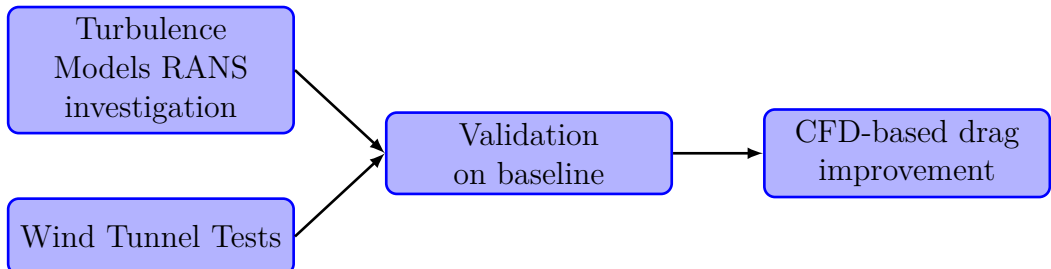


Figure 1.1: Thesis workflow.

1. Introduction

2

CFD theory

2.1 Reynolds Averaged Navier–Stokes

In Computational Fluid Dynamics (CFD), fluid motion is predicted by solving the discrete form of the governing equations. The choice of the mathematical model dictates the computational cost and resolution, spanning from Direct Numerical Simulation (DNS) to Reynolds-Averaged Navier-Stokes (RANS). DNS is the most accurate approach as it resolves all turbulent scales, from the largest integral length scales L down to the smallest dissipative Kolmogorov scales η . However, to capture these smallest scales, the number of required grid points N scales rapidly with the Reynolds number:

$$N \approx Re^{9/4}$$

For a typical road vehicle, where the Reynolds number is in the order of 10^6 to 10^7 , the grid requirements for DNS are currently prohibitive for industrial applications. As a reference a very large mesh grid could be of the order of 10^9 cells, as the case published by Dr. Lehmann [15]. To overcome these limitations, RANS models are utilised. The RANS models require smaller cell number because they do not solve small scales, so there is no need for such small grid.

Starting from Navier-Stokes equations

$$\frac{\partial \rho}{\partial t} + \frac{\partial(\rho u_j)}{\partial x_j} = 0 \quad (2.1)$$

$$\rho \left(\frac{\partial u_i}{\partial t} + u_j \frac{\partial u_i}{\partial x_j} \right) = - \frac{\partial p}{\partial x_i} + \frac{\partial \tau_{ij}}{\partial x_j} + \rho f_i \quad (2.2)$$

$$\tau_{ij} = \mu \left(\frac{\partial u_i}{\partial x_j} + \frac{\partial u_j}{\partial x_i} \right) - \frac{2}{3} \mu \frac{\partial u_k}{\partial x_k} \delta_{ij} \quad (2.3)$$

where ρ is the density and u_i the i -th component of the velocity vector of the fluid particle. The Equation 2.1 is the continuity and the Equation 2.2 the momentum conservation. Considering the incompressible and constant μ case 2.2 becomes

2. CFD theory

$$\frac{\partial u_i}{\partial t} + u_j \frac{\partial u_i}{\partial x_j} = - \frac{1}{\rho} \frac{\partial p}{\partial x_i} + \nu \frac{\partial^2 u_i}{\partial x_j \partial x_j} \quad (2.4)$$

so now it is possible to define the Reynolds decomposition and time average operator as

$$u_i = \bar{u}_i + u'_i \quad (2.5)$$

$$p = \bar{p} + p' \quad (2.6)$$

$$\bar{u}_i = \frac{1}{T} \int_t^{t+T} u_i(\tau) d\tau \quad (2.7)$$

$$u'_i = u_i - \bar{u}_i \quad (2.8)$$

applying the decomposition to Equation 2.4 and assuming statistically steady flow, i.e. $\partial()/\partial t = 0$, we get

$$\bar{u}_j \frac{\partial \bar{u}_i}{\partial x_j} = - \frac{1}{\rho} \frac{\partial \bar{p}}{\partial x_i} + \nu \frac{\partial^2 \bar{u}_i}{\partial x_j \partial x_j} - \frac{\partial \bar{u}'_i \bar{u}'_j}{\partial x_j} \quad (2.9)$$

where the term $\bar{u}'_i \bar{u}'_j$, called *Reynolds stress tensor (RSS)*, describes mean effect of turbulence. This set of equations is not close since the averaging operation has introduced as unknowns the six independent components of the RSS. A possible approach is to write the transport equation for the RSS itself and compute directly all tensor components, such method is the most accurate turbulent model as well as the most time consuming. [16].

$$\bar{u}_k \frac{\partial (\bar{u}'_i \bar{u}'_j)}{\partial x_k} = P_{ij} + \Phi_{ij} - \varepsilon_{ij} + D_{ij} \quad (2.10)$$

$$P_{ij} = - \left(\bar{u}'_i \bar{u}'_k \frac{\partial \bar{u}_j}{\partial x_k} + \bar{u}'_j \bar{u}'_k \frac{\partial \bar{u}_i}{\partial x_k} \right) \quad (2.11)$$

$$\Phi_{ij} = - \frac{1}{\rho} \left(\bar{u}'_i \frac{\partial p'}{\partial x_j} + \bar{u}'_j \frac{\partial p'}{\partial x_i} \right) \quad (2.12)$$

$$\varepsilon_{ij} = 2\nu \frac{\partial \bar{u}'_i}{\partial x_k} \frac{\partial \bar{u}'_j}{\partial x_k} \quad (2.13)$$

$$D_{ij} = \frac{\partial}{\partial x_k} \left[\nu \frac{\partial \bar{u}'_i \bar{u}'_j}{\partial x_k} - \frac{1}{\rho} \bar{u}'_i p' \delta_{jk} - \frac{1}{\rho} \bar{u}'_j p' \delta_{ik} + \frac{1}{2} \bar{u}'_i \bar{u}'_j \bar{u}'_k \right] \quad (2.14)$$

Another possible approach use the Boussinesq eddy viscosity model to close the problem

$$\overline{u'_i u'_j} = -\nu_t \left(\frac{\partial \overline{u_i}}{\partial x_j} + \frac{\partial \overline{u_j}}{\partial x_i} \right) + \frac{2}{3} k \delta_{ij} \quad (2.15)$$

where ν_t is called turbulent viscosity and $k = \frac{1}{2} \overline{u'_i u'_i}$ is the turbulent kinetic energy. As a direct consequence of this assumption, the model fails to predict the anisotropy in simple configurations such as fully developed plane channel flows [17]. Re-writing Equation 2.9 using Equation 2.15 we get

$$\overline{u_j} \frac{\partial \overline{u_i}}{\partial x_j} = -\frac{1}{\rho} \frac{\partial}{\partial x_i} \left(\overline{p} + \frac{2}{3} k \right) + \frac{\partial}{\partial x_j} \left[(\nu + \nu_t) \left(\frac{\partial \overline{u_i}}{\partial x_j} + \frac{\partial \overline{u_j}}{\partial x_i} \right) \right] \quad (2.16)$$

where $\nu_{eff} = \nu + \nu_t$ is the effective turbulent viscosity. Finally the problem can be close with two additional transport equation, one for the turbulent kinetic energy k and one for the turbulent dissipation rate ε and an explicit expression for ν_t

$$\overline{u_j} \frac{\partial k}{\partial x_j} = \frac{\partial}{\partial x_j} \left[\left(\nu + \frac{\nu_t}{\sigma_k} \right) \frac{\partial k}{\partial x_j} \right] + P_k - \varepsilon \quad (2.17)$$

$$\varepsilon = 2\nu \overline{S'_{ij} S'_{ij}} \quad S'_{ij} = \frac{1}{2} \left(\frac{\partial u'_i}{\partial x_j} + \frac{\partial u'_j}{\partial x_i} \right) \quad (2.18)$$

$$\overline{u_j} \frac{\partial \varepsilon}{\partial x_j} = \frac{\partial}{\partial x_j} \left[\left(\nu + \frac{\nu_t}{\sigma_\varepsilon} \right) \frac{\partial \varepsilon}{\partial x_j} \right] + C_{\varepsilon 1} \frac{\varepsilon}{k} P_k - C_{\varepsilon 2} \frac{\varepsilon^2}{k} \quad (2.19)$$

$$\nu_t = C_\mu \frac{k^2}{\varepsilon} \quad (2.20)$$

$$P_k = 2\nu_t S_{ij} S_{ij} \quad (2.21)$$

$$S_{ij} = \frac{1}{2} \left(\frac{\partial \overline{u_i}}{\partial x_j} + \frac{\partial \overline{u_j}}{\partial x_i} \right) \quad (2.22)$$

C_μ is the damping model coefficient, $C_{\varepsilon 1}$ are $C_{\varepsilon 2}$ model constants, σ_k is the Prandtl-Schmidt number for diffusion coming from gradient-diffusion hypothesis:

$$-\frac{1}{2} \overline{u'_i u'_i u'_k} - \frac{\overline{p' u'_k}}{\rho} \approx \frac{\nu_t}{\sigma_k} \frac{\partial k}{\partial x_k} \quad (2.23)$$

This model is called $k - \varepsilon$ model and was first derived by Launder and Spalding [18], further improvements to the model have been proposed over the years, yielding to a huge number of different turbulent models. This thesis discusses three of the most common and advanced methods used today. It is important to emphasise from the

2. CFD theory

outset that these models all suffer from the same chronic error. They describe the fluid dynamic behaviour only as time averaged, whereas a turbulent system is highly characterized by unsteady phenomena, such as separation, vortex shading, recirculation, etc. Furthermore, they do not resolve the turbulence, either on a small or on a large scale. The choice was dictated by the limited computational resources available.

It is relevant to mention the existence of models of intermediate accuracy between DNS and RANS, often used in industrial applications. Detached Eddy Simulation and Delayed Detached Eddy Simulation (DES and DDES). Even these more accurate methods were ruled out early on due to limited computing resources and are not covered in this work.

2.2 Turbulent models in Star-CCM+

There are four major classes of RANS turbulence models currently in Simcenter Star-CCM+. The following informations are taken from Simcenter Star-CCM+ User Guide 2502. First the Spalart-Allmaras models are good choices for applications in which the boundary layers are largely attached and separation is mild if it occurs. Typical examples would be flow over a wing, fuselage or other aerospace external-flow applications, so it is not suitable for this thesis purpose.

The second class, $k-\varepsilon$ models, provide a good compromise between robustness, computational cost and accuracy. They are generally well suited to industrial-type applications that contain complex recirculation. Third class, $k-\omega$ models are similar to $k-\varepsilon$ models in that two transport equations are solved, but differ in the choice of the second transported turbulence variable. The performance differences are likely to be a result of the subtle differences in the models, rather than a higher degree of complexity in the physics being captured. These models have seen most applications in the aerospace industry.

Fourth, Reynolds Stress Transport models are the most complex and computationally expensive RANS models offered in Simcenter Star-CCM+. They are recommended for situations in which the turbulence is strongly anisotropic, such as the swirling flow in a cyclone separator, so since I do not have such needs and computational resources are limited I discarded this model.

Following Star-CCM+ 2502 best practices for external automotive aerodynamics I have selected three specific turbulent models, under the two selected classes: Realizable $k-\varepsilon$ two layers treatment, Lag EB $k - \varepsilon$ two layers treatment and $k-\omega$ SST low y^+ treatment.

In Simcenter Star-CCM+ the two-layer approach is an alternative to the low-Reynolds number approach that allows the $k-\varepsilon$ model to be applied in the viscous-affected layer (including the viscous sub-layer and the buffer layer). In this approach, the computation is divided into two layers. In the layer next to the wall, the turbulent dissipation rate ε and the turbulent viscosity μ_t are specified as functions of wall distance. The values of ε specified in the near-wall layer are blended smoothly with the values computed from solving the transport equation far from the wall. The equation for the turbulent kinetic energy is solved across the entire flow domain. This explicit specification of ε and μ_t is arguably no less empirical than the damping function approach, and the results are often as good or better.

In Simcenter Star-CCM+, the two-layer formulations work with either low-Reynolds number type meshes $y^+ \sim 1$ or wall-function type meshes $y^+ > 30$.

Please note that the mathematical models below contain terms with time derivatives. This choice was made for the sake of completeness. The complete formulation contained in the papers in which they were first presented is reported, even though the simulations conducted are steady-state.

2.2.1 Realizable $k - \varepsilon$

The Realizable $k-\varepsilon$ model contains a new transport equation for the turbulent dissipation rate ε [19], respect to the standard $k - \varepsilon$. Also, a variable damping function f_μ , expressed as a function of mean flow and turbulence properties, is applied to a critical coefficient of the model C_μ . This procedure lets the model satisfy certain mathematical constraints on the normal stresses consistent with the physics of turbulence (realizability). This concept of a damped C_μ is also consistent with experimental observations in boundary layers. The Realizable Two-Layer $k-\varepsilon$ model combines the Realizable $k-\varepsilon$ model with the two-layer approach. The coefficients in the models are identical, but the model gains the added flexibility of an all-wall treatment. The formulation of the model is shown below:

$$\frac{\partial(\rho k)}{\partial t} + \frac{\partial(\rho k u_j)}{\partial x_j} = \frac{\partial}{\partial x_j} \left[\left(\mu + \frac{\mu_t}{\sigma_k} \right) \frac{\partial k}{\partial x_j} \right] + P_k - \rho (\varepsilon - \varepsilon_0) + S_k, \quad (2.24)$$

$$\frac{\partial(\rho \varepsilon)}{\partial t} + \frac{\partial(\rho \varepsilon u_j)}{\partial x_j} = \frac{\partial}{\partial x_j} \left[\left(\mu + \frac{\mu_t}{\sigma_\varepsilon} \right) \frac{\partial \varepsilon}{\partial x_j} \right] + \frac{1}{T_e} C_{\varepsilon 1} P_\varepsilon - C_{\varepsilon 2} f_2 \rho \left(\frac{\varepsilon}{T_e} - \frac{\varepsilon_0}{T_0} \right) + S_\varepsilon, \quad (2.25)$$

$$\mu_t = \rho C_\mu f_\mu k T_e, \quad T_e = \frac{k}{\varepsilon}. \quad (2.26)$$

In these equations, the terms on the left-hand side represent the transient and convective transport of the turbulent variables. Above terms with the time derivative appear for the sake of generality. In the context of this thesis, which performs

2. CFD theory

steady-state RANS simulations, the mean flow statistics are assumed to be time-independent. Consequently, these transient terms vanish (are equal to zero) and are only active in the case of Unsteady-RANS (URANS) simulations.

On the right-hand side, the first term represents the diffusion, governed by the turbulent Prandtl numbers σ_k and σ_ε . P_k denotes the production of turbulent kinetic energy due to mean velocity gradients, while ε represents its dissipation. A key distinction of the Realizable model, as proposed by Shih et al. [19], lies in the coefficients. $C_{\varepsilon 1}$ is not constant but is a function of the mean strain rate, allowing the model to better predict the spreading rate of planar and round jets. Furthermore, the eddy viscosity coefficient C_μ is variable, depending on the mean flow deformation and rotation. This ensures that the model satisfies the mathematical constraints of *realizability* (positivity of normal Reynolds stresses), making it superior to the Standard $k - \varepsilon$ model for flows involving strong pressure gradients, separation, and recirculation. Finally, the terms f_μ and f_2 are damping functions introduced by the two-layer wall treatment implemented in Star-CCM+. These functions blend the fully turbulent core flow with the viscosity-affected near-wall layer, allowing for more accurate solutions even when the mesh resolves the viscous sub-layer ($y^+ \approx 1$).

2.2.2 Lag EB $k - \varepsilon$

Conventional two-equation eddy-viscosity RANS closures such as Spalart–Allmaras [20] and other $k - \varepsilon$ models struggle to predict stress–strain misalignment and associated non-equilibrium phenomena, with the tendency to over-predict the k term. To address these limitations, Lardeau and Billard [21] developed an elliptic-blending lag model, incorporating the angle between stress–strain components by augmenting a baseline three-equation formulation with an analytically derived transport equation for a lag parameter ϕ , combining the elliptic-blending RSM of Manceau and Hanjalić [22] with the stress-strain lag concept originally proposed by Revell et al. [23]. The key benefits include significantly enhanced turbulent kinetic energy production in regions of principal-axis misalignment, markedly improved prediction of skin-friction and recirculation length in separated flows, and robust performance under curvature, rotation and three-dimensional high-lift configurations, as demonstrated against LES and experimental benchmarks [21]. Full model formulation is shown below:

$$\frac{\partial k}{\partial t} + u_j \frac{\partial k}{\partial x_j} = P - \varepsilon + \frac{\partial}{\partial x_j} \left[\left(\frac{\nu}{2} + \frac{\nu_t}{\sigma_k} \right) \frac{\partial k}{\partial x_j} \right], \quad (2.27)$$

$$\frac{\partial \varepsilon}{\partial t} + u_j \frac{\partial \varepsilon}{\partial x_j} = C_{\varepsilon 1} \frac{P \varepsilon}{k} - C_{\varepsilon 2}^* \frac{\varepsilon^2}{k} + \frac{\partial}{\partial x_j} \left[\left(\frac{\nu}{2} + \frac{\nu_t}{\sigma_\varepsilon} \right) \frac{\partial \varepsilon}{\partial x_j} \right], \quad (2.28)$$

$$\frac{\partial \phi}{\partial t} + u_j \frac{\partial \phi}{\partial x_j} = (1 - \alpha^3) f_w + \alpha^3 f_h - C_{p1} \frac{P}{k} \phi + \frac{\partial}{\partial x_j} \left[\left(\frac{\nu}{2} + \frac{\nu_t}{\sigma_\phi} \right) \frac{\partial \phi}{\partial x_j} \right], \quad (2.29)$$

$$L^2 \frac{\partial^2 \alpha}{\partial x_j \partial x_j} = \alpha - 1 \quad (2.30)$$

with following definitions:

$$E = -2 C_k \nu \nu_t (1 - \alpha)^3 \left(\frac{\partial \|S_{ij} n_j\| n_k}{\partial x_k} \right)^2, \quad (2.31)$$

$$f_h = C_w^* \phi \frac{\varepsilon}{k}, \quad (2.32)$$

$$f_w = \left(\tilde{C}_1 + C_1^* \frac{P}{\varepsilon} \right) \frac{\phi}{\tau} + C_{P2} \phi S + C_{P3} \frac{1}{\tau} + \tau_s M_{ij} S_{ij}, \quad (2.33)$$

$$\tau_s = \tau \max(\eta^2, 1), \quad \tau = \sqrt{\left(\frac{k}{\varepsilon} \right)^2 + C_t \frac{\nu}{\varepsilon}}, \quad (2.34)$$

$$L = C_L \sqrt{\left(\frac{k}{\varepsilon} \right)^3 + C_\eta^2 \frac{\nu^3}{\varepsilon}}. \quad (2.35)$$

equations coefficients are shown in table 2.1.

σ_k	σ_φ	σ_ε	C_μ	C_t	$C_{\varepsilon 1}$	$C_{\varepsilon 2}$	C_k	C_L	C_η	C_{cr1}
1	1	1.15	0.22	4	1.44	1.86	2.3	0.164	75	0.4

Table 2.1: Lag EB turbulent model coefficients

2.2.3 SST $k - \omega$

The $k-\omega$ turbulence model is a two-equation model that solves transport equations for the turbulent kinetic energy ε and the specific dissipation rate ω in order to determine the turbulent eddy viscosity. One reported advantage of the $k-\omega$ model over the $k-\varepsilon$ model is its improved performance for boundary layers under adverse pressure gradients. Perhaps the most significant advantage, however, is that it may be applied throughout the boundary layer, including the viscous-dominated region, without further modification.

2. CFD theory

The biggest disadvantage of the $k-\omega$ model, in its original form, is that boundary layer computations are sensitive to the values of in the free-stream.. The problem of sensitivity to free-stream/inlet conditions was addressed by Menter [24], who recognized that the ε transport equation from the Standard $k-\varepsilon$ model could be transformed into an ω transport equation by variable substitution.

The transformed equation looks similar to the one in the Standard $k-\omega$ model, but adds an additional non-conservative cross-diffusion term containing the dot product $\nabla k \cdot \nabla \omega$. Inclusion of this term in the ω transport equation potentially makes the $k-\omega$ model give identical results to the $k-\varepsilon$ model. Menter suggested using a blending function that would include the cross-diffusion term far from walls, but not near the wall. This approach effectively blends a $k-\varepsilon$ model in the far-field with a $k-\omega$ model near the wall.

Menter also introduced a modification to the linear constitutive equation and named the model containing this modification the SST (shear-stress transport) $k-\omega$ model. However, the linear relation between the Reynolds stresses and the mean strain rate tends to strongly under predict the anisotropy of turbulence. Turbulence is anisotropic in most complex flows—for example in strong swirl, streamline curvature, shear layer, or boundary layer flows.

Full formulation of the two equation model is shown below:

$$\frac{\partial(\rho k)}{\partial t} + \frac{\partial(\rho k u_j)}{\partial x_j} = \tau_{ij} \frac{\partial u_i}{\partial x_j} - \beta^* \rho \omega k + \frac{\partial}{\partial x_j} \left[(\mu + \sigma_k \mu_t) \frac{\partial k}{\partial x_j} \right], \quad (2.36)$$

$$\begin{aligned} \frac{\partial(\rho \omega)}{\partial t} + \frac{\partial(\rho \omega u_j)}{\partial x_j} &= \gamma \frac{\nu_t}{\mu_t} \tau_{ij} \frac{\partial u_i}{\partial x_j} - \beta \rho \omega^2 + \frac{\partial}{\partial x_j} \left[(\mu + \sigma_\omega \mu_t) \frac{\partial \omega}{\partial x_j} \right] \\ &+ 2(1 - F_1) \rho \sigma_\omega \frac{1}{\omega} \frac{\partial k}{\partial x_j} \frac{\partial \omega}{\partial x_j} \end{aligned} \quad (2.37)$$

all the parameters should be calculated as follow:

$$\varphi = F_1 \varphi_1 + (1 - F_1) \varphi_2 \quad (2.38)$$

where ϕ_i is the i-set of constants:

$$\begin{aligned} \sigma_{k1} &= 0.85, & \sigma_{\omega1} &= 0.5, & \beta_1 &= 0.0750, & a_1 &= 0.31 \\ \beta^* &= 0.09, & \kappa &= 0.41, & \gamma_1 &= \beta_1 / \beta^* - \sigma_{\omega1} \kappa^2 / \sqrt{\beta^*} \end{aligned}$$

$$\begin{aligned}\sigma_{k2} &= 1.0, & \sigma_{\omega 2} &= 0.856, & \beta_2 &= 0.0828 \\ \beta^* &= 0.09, & \kappa &= 0.41, & \gamma_2 &= \beta_2/\beta^* - \sigma_{\omega 2}\kappa^2/\sqrt{\beta^*}\end{aligned}$$

with the following definitions:

$$F_1 = \tanh(\arg_1^4) \quad (2.39)$$

$$\arg_1 = \min \left[\max \left(\frac{\sqrt{k}}{0.09\omega y}; \frac{500\nu}{y^2\omega} \right); \frac{4\rho\sigma_{\omega 2}k}{CD_{k\omega}y^2} \right] \quad (2.40)$$

$$\tau_{ij} = \mu_t \left(\frac{\partial u_i}{\partial x_j} + \frac{\partial u_j}{\partial x_i} - \frac{2}{3} \frac{\partial u_k}{\partial x_k} \delta_{ij} \right) - \frac{2}{3} \rho k \delta_{ij} \quad (2.41)$$

where y is the distance to the next surface and $CD_{k\omega}$ is the positive portion of the cross-diffusion term of the second equation of 2.36:

$$CD_{k\omega} = \max \left(2\rho\sigma_{\omega 2} \frac{1}{\omega} \frac{\partial k}{\partial x_j} \frac{\partial \omega}{\partial x_j}, 10^{-20} \right) \quad (2.42)$$

and the eddy viscosity model is:

$$\nu_t = \frac{a_1 k}{\max(a_1 \omega; \Omega F_2)} \quad (2.43)$$

$$F_2 = \tanh(\arg_2^2) \quad (2.44)$$

$$\arg_2 = \max \left(2 \frac{\sqrt{k}}{0.09\omega y}; \frac{500\nu}{y^2\omega} \right) \quad (2.45)$$

2.2.4 Models summary

In Table 2.2 the most relevant features for each model, the advantages and disadvantages are listed. The primary source of information for pros and cons is Siemens Best Practice document 2502 for vehicle aerodynamics.

2. CFD theory

Model and Key Characteristics	Advantages	Limitations
Realizable $k-\varepsilon$ [19] <ul style="list-style-type: none"> • Variable damping coefficient C_μ based on mean strain/rotation. • New transport equation for ε. 	<ul style="list-style-type: none"> • Satisfies mathematical realizability constraints (prevents negative normal stresses). • Corrects turbulent kinetic energy production in stagnation region compared to standard $K-\varepsilon$ formulation, provides steady flow field, good convergence behavior and delivers great trends 	<ul style="list-style-type: none"> • Few studies showed late separation and some cases miss lift prediction.
Lag EB $k-\varepsilon$ [21] <ul style="list-style-type: none"> • Elliptic Blending (EB) for near-wall anisotropy. • Lag parameter accounts for stress-strain misalignment. 	<ul style="list-style-type: none"> • Resolves "stagnation point anomaly". • Superior prediction of separation onset and recirculation lengths. • Takes into account the misalignment of stress and strain-rate within an eddy-viscosity model (important for a vortex traveling downstream), showed excellent convergence behavior even for challenging cases and delivers great results 	<ul style="list-style-type: none"> • Higher computational cost due to additional transport equations. • Might be a bit more unstable than $k-\varepsilon$ or $k-\omega$ SST models.
SST $k-\omega$ [24] <ul style="list-style-type: none"> • Zonal blending: $k-\omega$ near-wall, $k-\varepsilon$ far-field. • Shear Stress Transport (SST) limiter. 	<ul style="list-style-type: none"> • Robust near-wall resolution without complex damping functions. • Excellent for boundary layers under adverse pressure gradients. 	<ul style="list-style-type: none"> • Tendency to over-predict turbulence in stagnation regions. • Assumes linear stress-strain relationship (isotropic).

Table 2.2: Comparative summary of the selected RANS turbulence models.

3

Methodology

3.1 pickup truck model

The ECARA research group has developed a standard pickup truck model that is representative of the mean market pickup truck model [25], the so-called Generic Truck Utility (GTU). The variant used in this work can be considered as de-featured, without internal flows and small details and with a flat floor, to be used as a baseline. In Figure 3.2 the de-featured version, left-hand side, is compared with the original ECARA model, right-hand side. This model comes from previous studies at the University of Chalmers, it has been provided as an .stl file and a physical scaled 1:10 3D printed model.

The model used as a baseline has two possible configurations, open bed and closed bed, hereafter OB and CB. The only difference is whether the deck is covered or not. They are the most common configuration on the market. In Figure 3.1 the two baseline configurations are shown. The model sizes are listed in Table 3.1.

Frontal Area	2.5 m^2
Overall Length (L)	5250 mm
Overall Width (W)	2200 mm
Overall Height (H)	1650 mm
Box to Cab Gap	20 mm

Table 3.1: Baseline dimensions. See Figure 3.1 as reference.

3.2 CFD domain and setup

A steady simulation was selected with half-body domain and symmetry boundary condition on plane of symmetry, in order to save computational resources ¹. It is

¹The body geometry is symmetrical

3. Methodology

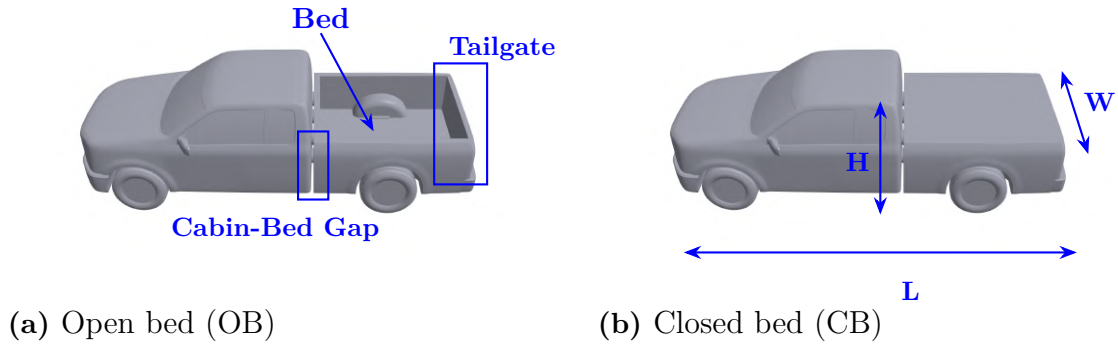


Figure 3.1: The two baseline configurations studied.

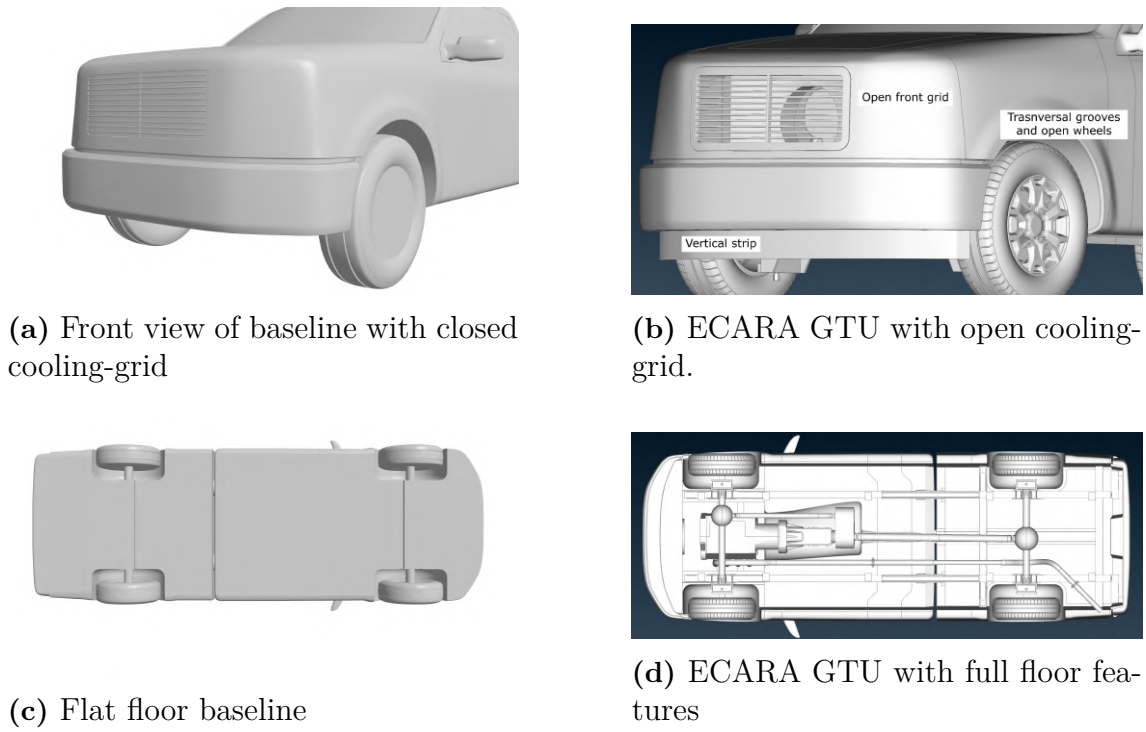


Figure 3.2: Differences between ECARA GTU 3.2b/3.2d and baseline model 3.2a/3.2c.

relevant to mention that the wake of a bluff body often exhibits a bistable or asymmetric vortex shedding, even with symmetric geometry [26,27]. Using the symmetric boundary condition, this transient is suppressed.

Figure 3.3 shows the fluid domain with measurements referring to the pickup dimensions. The boundary conditions applied are: symmetry on top, side and symmetry planes, velocity inlet on front plane, pressure outlet on back plane, and moving ground with a tangential velocity imposed on the ground plane.

To model rotating wheels, a tangential velocity has been set on wheels and treated as a solid wall, with a local coordinate system in the centre of rotation. In Table 3.2 relevant reference values for the ambient simulation condition are listed.

The Reynolds number definition used is: $Re = \frac{uL}{\nu}$ with L the length of the pickup truck body.

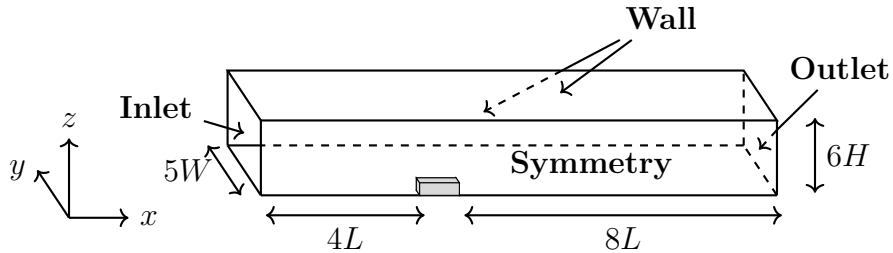


Figure 3.3: Domain for half body car, L length, H height and W width of the pickup.

Inlet velocity	Ref. pressure	Air density	Reynolds No.
30 m/s	1 atm	1.18415 kg/m ³	10 ⁷

Table 3.2: Simulation settings.

3.3 Mesh and convergence

To establish a valid mesh, since my computational resources were limited, the workflow shown in Figure 3.4 was adopted. Before starting, I made the assumption that once a valid mesh is obtained for OB case, i.e. for which the numerical results are mesh independent, it can be used with the same parameters for CB case.

Using the OB configuration, a single turbulence model was selected, the Lag EB k- ε , to carry out mesh convergence study. Choosing a $y^+ > 30$ I conduct a mesh

3. Methodology

convergence study establishing a valid volume mesh. Next, if necessary, I can increase the number of prism layers to reduce y^+ to 1 or lower, depending on the turbulence model used and the desired results.

Notice that a triangular surface remesh is performed in order to increase the surface quality before computing the volume mesh. The operation can be performed with the Star-CCM+ surface remesher tool.

The mesh type chosen is hexaedral mesh, calculated with trimmed cell mesher of Star-CCM+, in accordance with Star-CCM+ external aerodynamics best practices. Figure 3.6a and 3.6b show the various refinement regions used. Particular attention has been made in the prism layer definition for high y^+ cases. Since the flow inside the bed and in the rear of the model is extremely slow, and this region is very large, to avoid having too many cells in the buffer layer region, I defined zones with different prism layers. The model surface is covered by a *standard region* with 4 layers and a *slow region* with 2 layers and different near wall layer thickness. In Figure 3.6c is possible to see the transition between these two prism layer regions, on the cabin roof, the standard one, and at the cabin rear the slow. In contrast, Figure 3.6d presents the case with uniform prism layer for low y^+ , in this case there is no need for two different prism layer structures, so it is uniform through the body.

The results of the convergence mesh study are shown in Figure 3.5, each C_D value is the average value of the last 500 iterations in the simulation, and the error bars correspond to the standard deviation over the same 500 iterations; a total number of 2000 iterations has been used. To assess the convergence of the drag coefficient value as a function of mesh refinement levels, I calculated the generalised Richardson extrapolation, following Roache [28]. This method provides an objective asymptotic approach to quantifying the uncertainty arising from grid discretization. The fundamental premise is that the discrete solution, f (the drag coefficient in this case), behaves as a power series in the grid spacing, h . By obtaining solutions on two distinct grids, a fine grid (f_1) and a coarse grid (f_2), with a refinement ratio $r = h_2/h_1$, the method approximates the exact continuum solution by eliminating the leading order error term. The method has some limitations, this extrapolation is only valid when the solution fall within the "asymptotic range". Strictly, this extrapolation assumes that the grid is sufficiently fine such that the leading order truncation error dominates, a condition known as the asymptotic range. If non-physical oscillations are present, this indicates the solution is outside this range, rendering the extrapolation unreliable.

From the results, it is possible to select the second-last mesh as the definitive one, since the error with respect to Richardson asymptotic value is smaller than the standard deviation of related C_D value. Minor oscillatory behaviour was observed in the finest grids, likely due to the inherent unsteady nature of the bluff-body aerodynamic which steady RANS cannot fully resolve. Final volume mesh parameters

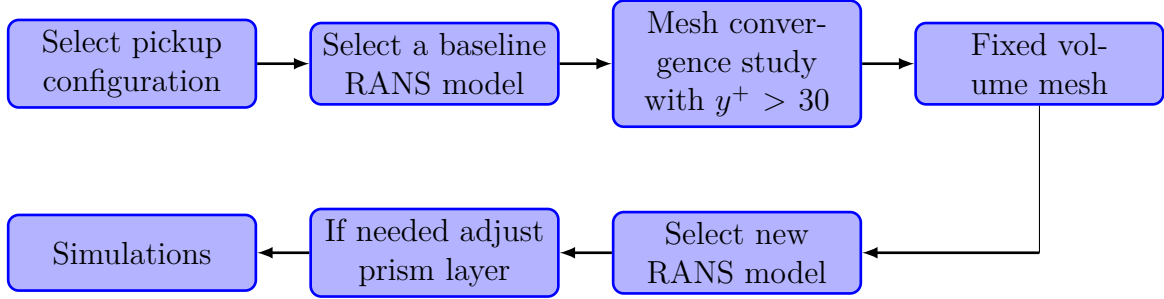


Figure 3.4: Workflow for mesh study.

are listed in Table 3.4 and in Table 3.3 are listed all the relevant information about prism layer for both low y^+ and high y^+ cases. Base size refers to the maximum edge size of a hexahedral cell; these cells belong to the regions furthest from the pickup.

As a prism layer quality check in Figure 3.8 is presented the y^+ field distribution through the body surface and in Figure 3.7 the relative histogram distribution normalized for body surface area, for both low and high y^+ . The bin frequency is calculated as:

$$Weighted\ Frequency = \frac{\sum_{i \in bin} |A_i|}{A_{tot}} \cdot 100\%$$

where A_i is the body surface area covered by the i th-mesh cells in the bin and A_{tot} is the total body surface area. In the high y^+ case the number of cells in the buffer region is relatively small and localized mainly at stagnation points, it is important since, as The Siemens reference explains the model struggle to predict the flow behaviour with many cells in the buffer layer. In the low y^+ case the number of cells with a value greater than 5 is completely negligible. Notice that the buffer layer is given for y^+ values between 5 and 30.

Parameter	Standard $y^+ > 30$	Slow region $y^+ > 30$	$y^+ \sim 1$
Number of layers	4	2	24
Near wall thickness	1 mm	2 mm	0.018 mm
Total thickness	5.368 mm	4.4 mm	7.0 mm

Table 3.3: Prism layer parameters.

3.4 Wind tunnel experiments

The wind tunnel used is owned by Chalmers University, it is a closed loop facility that operates at a maximum speed of $63m/s$ thanks to a $170kW$ electric motor and

3. Methodology

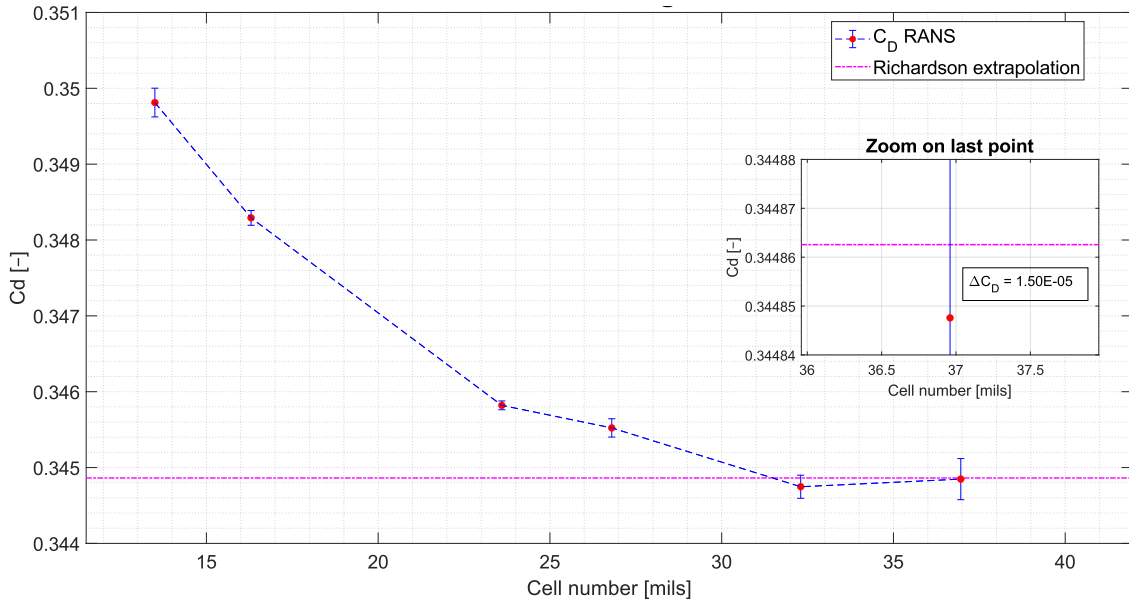


Figure 3.5: Mesh sensitivity level study.

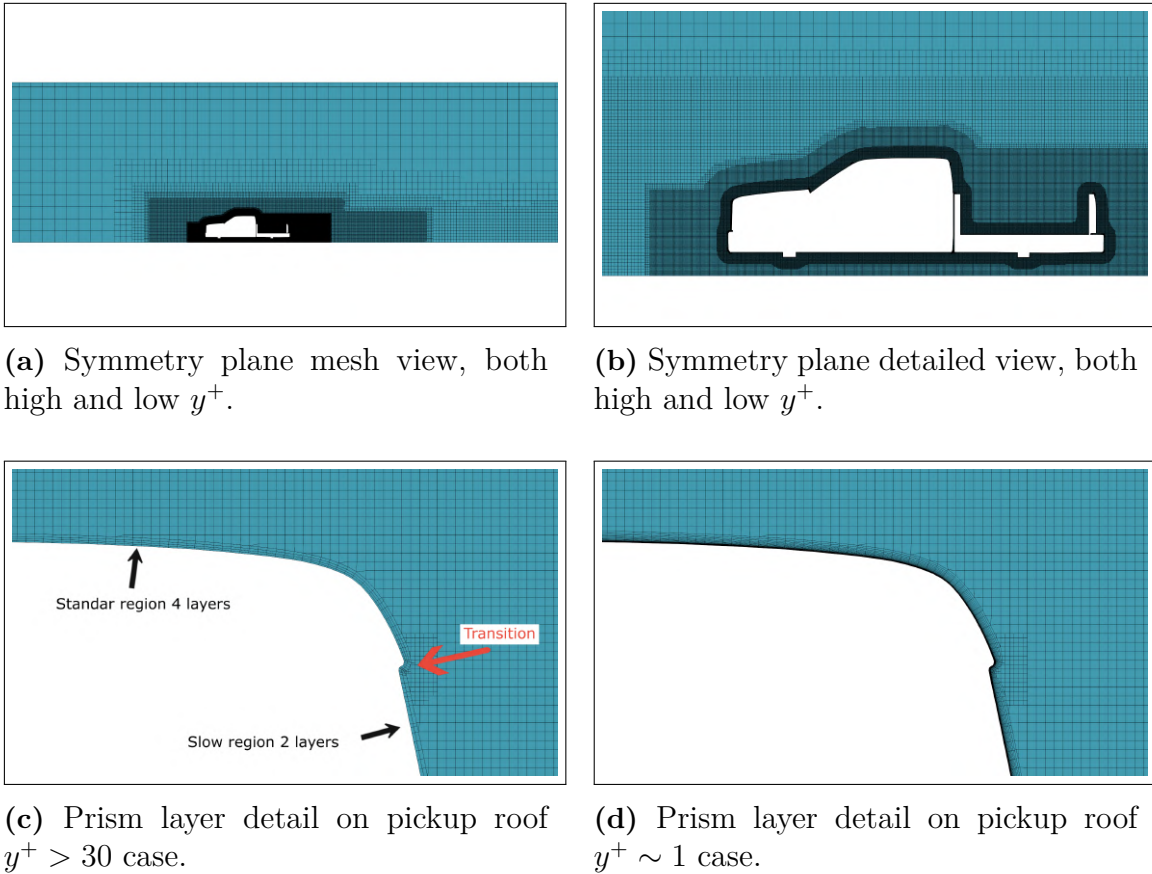


Figure 3.6: Selected mesh structure and details, with differences in prism layer structure between high y^+ and low y^+ treatment.

Region	Cells base size
Base	740 mm
Coarse box	5.5% of base
Coarse offset	2.0% of base
Coarse offset	1.0% of base
Fine offset	1.0% of base

Table 3.4: Selected volume mesh parameters.

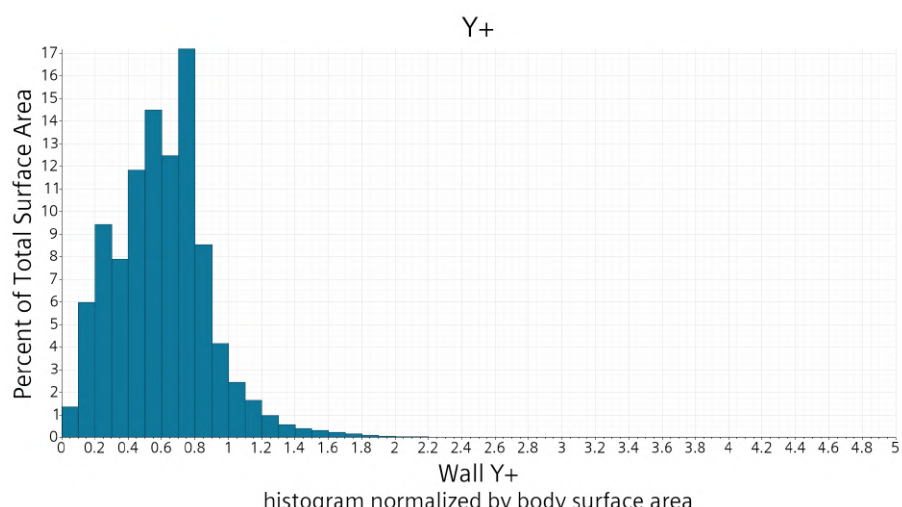
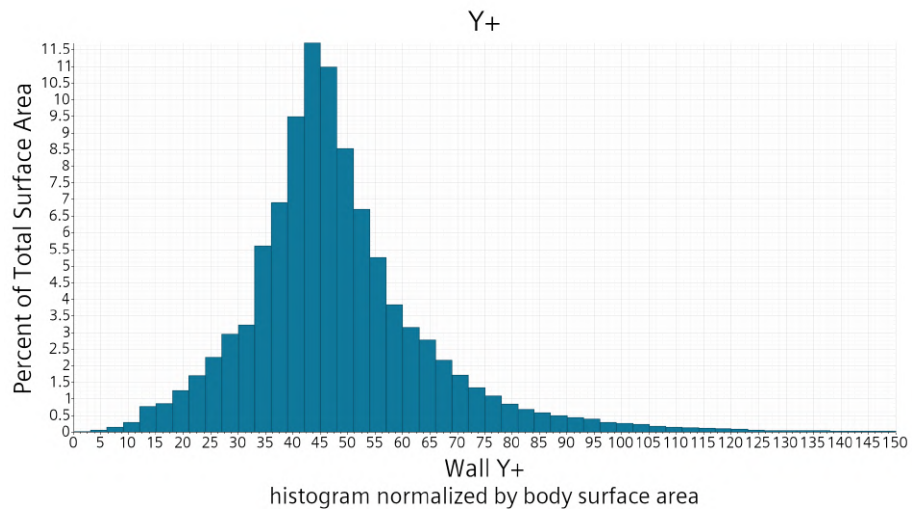


Figure 3.7: Histogram distribution of y^+ value normalized by body surface area.

3. Methodology

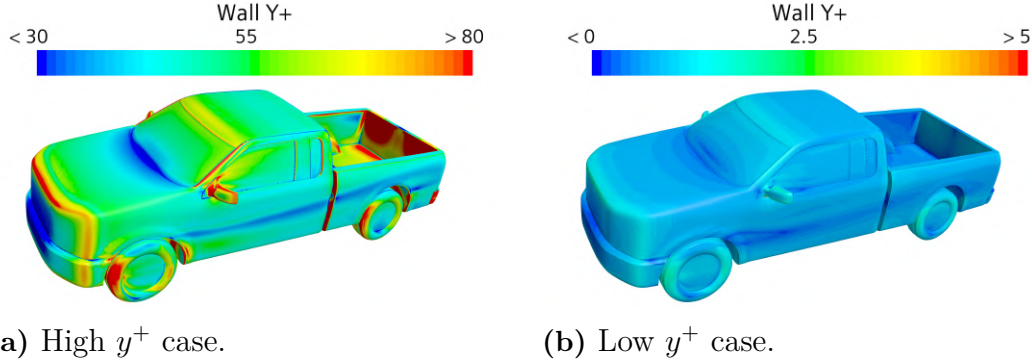


Figure 3.8: y^+ field distribution.

six blades fan. The test section is 3m in length with $2.25m^2$ cross section of the test section. The wind tunnel is equipped with a, already calibrated, 6-DOF balance, i.e. able to measure 3 mutually orthogonal moments and 3 mutually orthogonal forces.

The model used for tests is a 3D printed scaled model 1:10 of the CAD version used in numerical investigation. Figure 3.9 shows the model mounted in the test section, equipped with tufts for flow visualization.

The following correction equation could be used to include the blockage effect on measured data

$$C_{D_{true}} = C_{D_{measur}} \left(1 - \frac{A}{S}\right)^{1.228} \quad (3.1)$$

where A is the frontal area of the pickup and S is the cross-section area of the test section².

A Reynolds sweep study is shown in Figure 3.10, it can be observed that the independence of C_D from the Reynolds number is reached above $45m/s$ but due to noise, power and safety limits all the following measurements will be made at $35m/s$.

It is important to emphasise the conditions under which the measurements were taken: the 1:10 scale model does not have rotating wheels, and the test section does not have a moving ground or boundary layer removal devices, moreover the Reynolds number is consistently different between simulations and scaled test, from 10^7 (simulations) to 10^6 (WT tests).

The drag force was acquired, for both open and closed bed configurations, for yaw angles β [0° , 5° , 10° , 15°]. For each β value, I measured the force five times with a sampling time of 2 seconds and a frequency of 1000 Hz. The error on β value is the standard deviation of a uniform distribution $\frac{\Delta x}{\sqrt{12}}$, with Δx as the instrument

²This equation comes from previous internal studies conducted at Chalmers University

sensitivity, 0.5° . The error on drag value is the standard deviation over multiple acquisitions. All these data will be presented and commented inside following chapters.

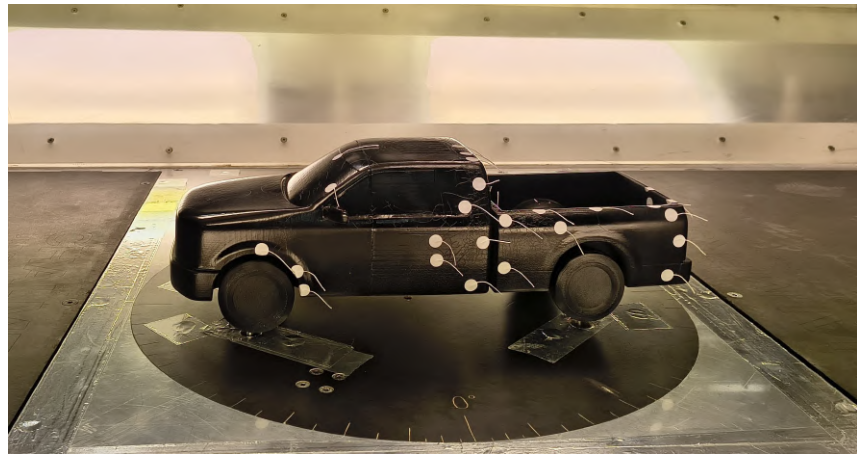


Figure 3.9: 1:10 scaled pickup model mounted in the wind tunnel test section.

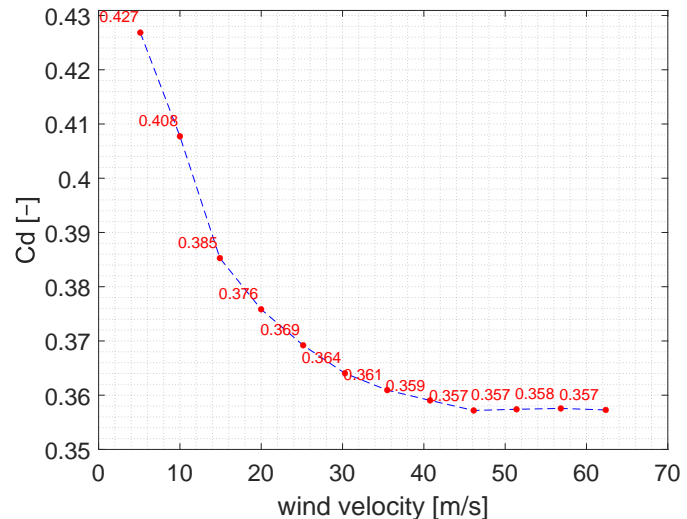


Figure 3.10: Reynolds sweep test.

3. Methodology

4

Results

4.1 Wind tunnel data

Figure 4.1 presents the results for drag coefficient as function of yaw angle β for both closed and open bed base line model.

Beyond $\beta = 0^\circ$, drag was also measured at $\beta \in \{5^\circ, 10^\circ, 15^\circ\}$ to estimate the Wind-Averaged Drag Coefficient, C_{DW} , following Howell et al [1]. This metric approximates real operating conditions and is more representative than C_D ($\beta = 0^\circ$), which neglects ambient cross-winds. C_{DW} is computed as a weighted sum of C_D values at prescribed yaw angles, Equation 4.1, using specific coefficients for the geographical regions, see Table 4.1.

$$C_{DW} = AC_{D0} + BC_{D5} + CC_{D10} + DC_{D15} \quad (4.1)$$

In Table 4.2 a comparison between the value obtained for C_D at $\beta = 0$ and the calculated C_{DW} is presented, with relative increment.

Region	A	B	C	E		Open bed	Closed bed
UK	0.48	0.42	0.10	0.014	C_D 0°	0.345	0.335
Europe	0.48	0.42	0.10	0.012	C_{DW}	0.381	0.366
USA	0.51	0.42	0.08	0.00	Increment	+10.4%	+9.25%

Table 4.1: Fitting coefficients for wind averaged drag, Howell et al. [1].

Table 4.2: Comparison between drag coefficient at $\beta = 0$ and C_{DW} value that estimate real wind conditions.

4.1.1 Comments on wind tunnel data

As already pointed out, the wind tunnel conditions do not match with numerical simulations. In particular, the presence of a boundary layer interference and static wheels have non-negligible effects on absolute drag values. Both OB and CB configurations are equally affected by this. This means that the absolute values from wind tunnel must be carefully treated and greater importance should be given to deltas, i.e. C_D variations as consequence of geometry modifications such as the ones between OB and CB.

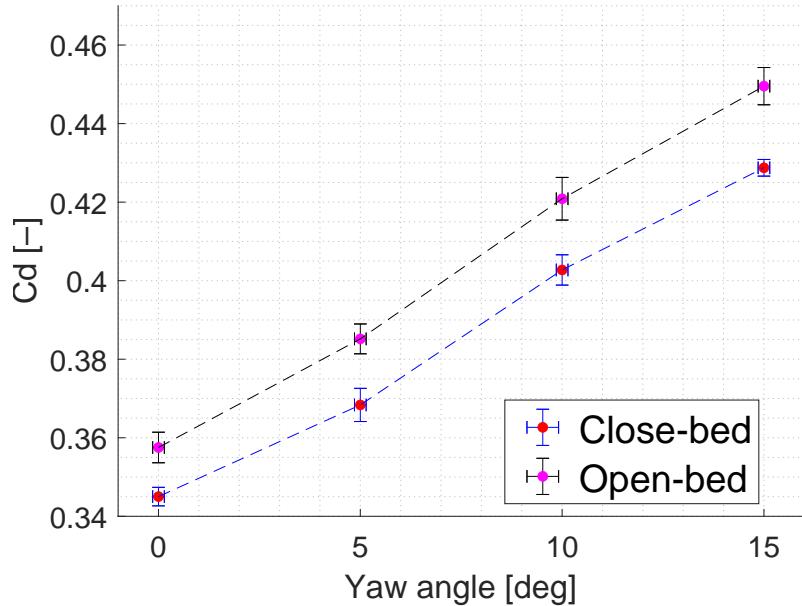


Figure 4.1: Drag coefficient for both OB and CB pickup baseline as function of β angle.

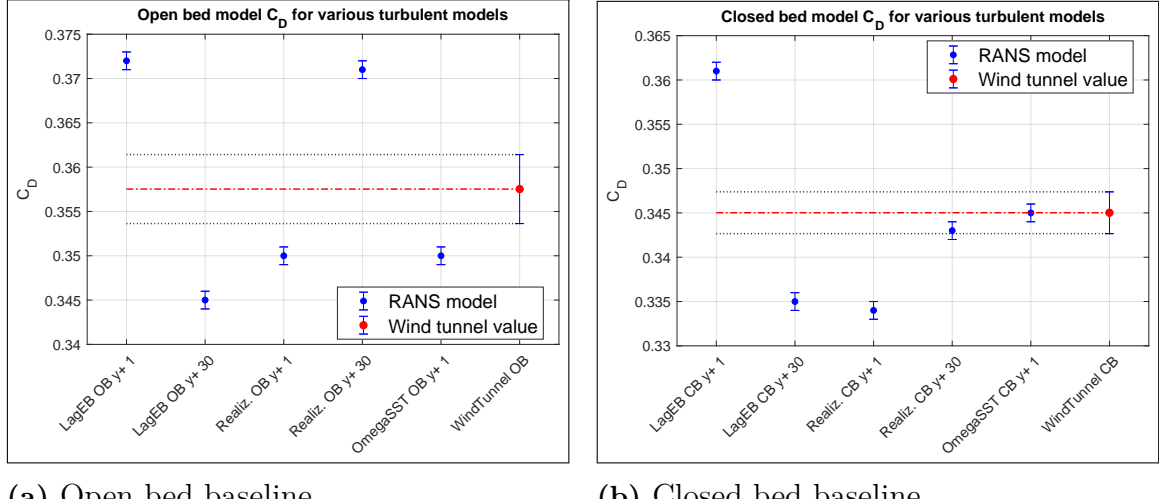
These data will be used as the validation and choice of the numerical turbulence model in the following section.

4.2 Turbulence models data

In this present section it is shown how the turbulence model and the y^+ target could affect the numerical results. In particular, I found a lack of knowledge in how the drag prediction change in case of pickup vehicle investigation. For this reason the following study cases have been computed and compared:

- Lag EB $k-\varepsilon$ with $y^+ \sim 1$;
- Lag EB $k-\varepsilon$ with $y^+ > 30$;
- Realizable $k-\varepsilon$ with $y^+ \sim 1$;
- Realizable $k-\varepsilon$ with $y^+ > 30$;
- SST $k-\omega$ with $y^+ \sim 1$.

The purpose of this analysis is not to find the most appropriate model in absolute terms, but to highlight how numerical results can vary and which model is closest to the wind tunnel data in my case study. Figure 4.2 reports two plots, one for each baseline configuration, OB and CB. The drag coefficient for each case listed previously and a reference point, the value coming from wind tunnel test for $\beta = 0$, is shown. To reduce systematic bias in absolute C_D predictions, the $\Delta C_D =$



(a) Open bed baseline.

(b) Closed bed baseline.

Figure 4.2: C_D value for each turbulence model, compared with wind tunnel value.

$C_{D_{\text{open bed}}} - C_{D_{\text{closed bed}}}$ ¹ is evaluated for each model. Because both configurations share the same test and numerical environments, ΔC_D . Is a more reliable basis for model comparison. The values obtained are reported in Figure 4.3. This procedure comes from the idea that a numerical simulation carried out via turbulent model has the objective to predict trends correctly, i.e. for a given body if it is modified the variations of relevant aerodynamic coefficients should be correctly predicted, but exhibits a bias error in absolute values for each specific case. The open and closed bed configurations differ only for the presence or not of a cover over the bed. So what I expect is each value of C_D , for each pickup configuration, either from numerical simulation or wind tunnel tests is affected by the same systematic error, so when the delta is calculated this systematic error present in both $C_{D_{\text{open bed}}}$ and $C_{D_{\text{closed bed}}}$ is cancelled out.

4.2.1 Comment on results

Comparing Figure 4.2b and Figure 4.2a, there is no evidence of a more accurate model than others, and it is difficult to draw conclusions. As already mentioned, this analysis focusses on deltas. Looking at Figure 4.3, and assuming the hypothesis previously made on ΔC_D , it is possible to assess that Lag EB turbulence model is the most reliable in delivering trends, even with high y^+ treatment. For this reason this RANS model, with $y^+ > 30$, from now on, is used for detailed aerodynamic investigation of baseline pickup and further models.

¹ C_{D_i} is the drag coefficient coming from a specific turbulence model

4. Results

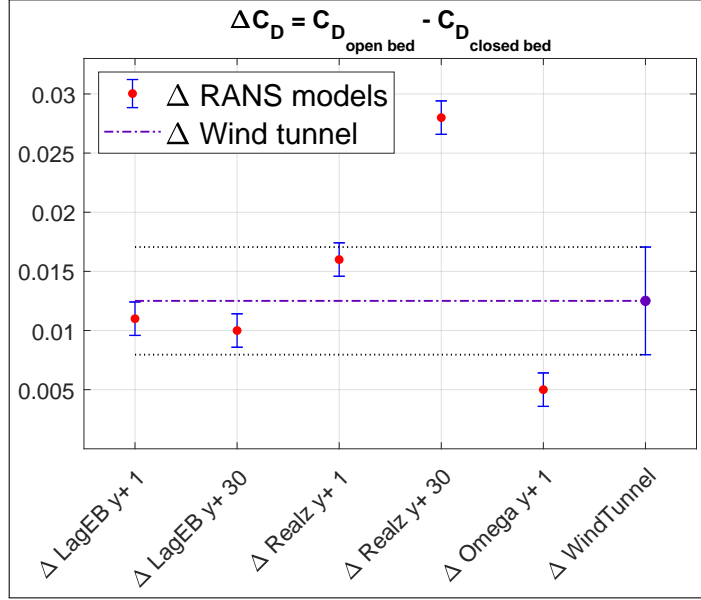


Figure 4.3: ΔC_D between open bed and closed bed configurations for all turbulence models compared to wind tunnel prediction.

4.3 Aerodynamic analysis: closed versus open bed

Using the Lag EB $k-\varepsilon$ model with $y^+ > 30$ for the two baseline configurations were analysed in detail, attempting to identify the sources of drag in order to develop solutions that could reduce the C_D . The simulation conditions are the same as previous and listed in Table 3.2 and the mesh used is the one discussed in Section 3.3.

Figure 4.4 shows the flow velocity field in two different XZ planes parallel to the longitudinal axis of the pickup. The first plane is the symmetry plane of the pickup, and the second one is located far from the centre. Figure 4.4 also compares the results for the OB case with the CB case. It is possible to see how the presence of the deck cover does not have huge effects on the wake structure, the two cases show similar wakes. It is important to note the presence of longitudinal vortices behind the tailgate in both configurations and the asymmetric structure of the wake with respect to the z-axis, slightly dominated by downwash behaviour.

This region of low-velocity flow seems to be slightly larger in the CB case, suggesting larger drag development.

Figures 4.5 and 4.6 show the distribution of the pressure coefficient on the front and rear surfaces of the pickup, respectively. From Figure 4.5, it can be deduced that opening or closing the bed has negligible effects on the differences in front pressure distribution between the OB and CB configurations. This qualitative ob-

servation can be quantitatively confirmed by Figure 4.7, where the accumulated drag force as a function of position x is calculated and plotted as a dimensionless drag coefficient for both OB and CB models. The red and blue lines, which indicate the increasing value of C_D along the pickup, are superimposed until the end of the passenger cabin. On the other hand, Figure 4.6 shows how the presence of the bed cover affects the base pressure distribution. It is interesting to observe that, at the rear of the cabin, the pressure is higher in the OB case, this means that one can expect a lower drag in that region with respect to the CB case. Looking at Figure 4.7, at $x = 3m$ immediately after the end of the cabin, it is possible to see a higher drag peak in the CB case, which is a consequence of the lower pressure acting on a backward-facing surface.

Figure 4.8 shows the flow that passes through the cabin-bed gap and how the flow is faster in the CB configuration. According to Bernoulli's principle, this local faster flow passing through a sort of "channel" results in a significant static pressure drop, explaining the lower pressure on the cabin back surface seen in Figure 4.6.

Despite the presence of this lower pressure zone, it is significant that the total drag coefficient is ultimately lower in the CB configuration (blue line).

C_D Open bed	C_D Closed bed
0.345	0.335

The reason for this result is the absence of deck cover in the OB case. In the OB, a low pressure area forms inside the bed and, as a result, a backward-facing surface, the leading edge, on which low pressure acts, thus generating drag. The development of drag in the rest of the pickup, until the tailgate, is similar between the two configurations. Then, the exposed tailgate gives in the OB case a drag recovery of ≈ 10 counts (0.01), confirming the observation made by Cooper [13] on the beneficial effect of having the tailgate up.

Closing the bed generally reduces drag, but introduces a local penalty at the cabin rear. There is great interest in investigating this area, in order to maintain, if possible, this gain until the end of the model.

There is a small gap between the cab and the deck, often found in real pickup vehicles, that is responsible for the pressure difference in the rear of the cab between the two configurations.

As already seen in Figure 4.6 the flow passing through the gap creates a pressure gradient in both configurations on the rear surface of the cabin, favouring the creation of two counter-rotating streamwise vortices (from now on RC-Vortex). Furthermore, the different pressure field between configurations influences the formation

4. Results

of these two vortices. Figure 4.9 shows the RC-Vortex behind the cabin. Comparing Figure 4.9a and Figure 4.9b, it can be seen that in the OB case, the vortex is more concentrated and located further away from the symmetrical one on the other side, compared to the CB case, where the two counter-rotating vortices are close to each other and much less concentrated.

To visualize the coherent turbulent structures, the Q-criterion method proposed by Jeong and Hussain [29] was employed. Figure 4.10 shows the isosurface for Q criterion with $Q = 1500$. The red surface identifies the locations of strong vortical structures, the regions close to the wall naturally indicate the boundary layer and elongated lobes downstream the presence of vortices. It is possible to underline once more that, in the OB case, the vortex at cabin rear corner is more concentrated with respect to the CB case. Lets notice how at the centre of cabin there is a region of vorticity due to the presence of, already discussed blowing, flow passing through the gap.

To identify losses regions, i.e. drag generations, it is possible to draw the isosurface for $C_{P_{tot}} = 0$. In fact, the definition of the Total Pressure Coefficient is $C_{P_{tot}} = \frac{P_{tot} - P_{\infty}}{1/2 \rho U_{\infty}^2}$ and is always 0 in an inviscid flow. When viscosity and turbulence are introduced, the energy is dissipated, P_{tot} drops, and $C_{P_{tot}}$ is negative. So, the isosurface identifies the boundary between the high-energy freestream and the low-energy wake. Physically, this volume can be interpreted as the "fluid body" or displacement shape "seen" by the external flow.

Figure 4.11 shows the two isosurfaces for the OB and CB configurations. Notice how the blue region in Figure 4.11a is bigger than the one in Figure 4.11b. This suggests greater losses and wake for the OB case, and is consistent with the higher drag coefficient observed.

A passenger vehicle must be stable and manoeuvrable in order to ensure comfortable driving on high-speed highways. The downforce generated by the vehicle is, therefore, of fundamental importance in this sector. A priori, one might expect a pickup truck to generate positive lift rather than downforce, due to the large low-pressure area above the deck. Figure 4.12 shows the lift coefficient accumulated along the pickup body for both the OB and the CB configurations. Negative values indicate downforce, while positive values indicate lift. As expected, both configurations have an overall positive C_L . It is important to note that the front half of the bodywork is substantially generating downforce, so the front wheels are not, reasonably, the critical elements for stability. On the contrary, the low pressure above the bed causes a reduction in the vertical force on the rear wheels, leading to possible stability problems. The closed bed configuration develops greater lift than the open bed one, in the region between $x = 3m$ and $x = 4m$, i.e. the region where the RC-Vortex is present. Referring to Figure 4.9, it is possible to draw a parallel between the size

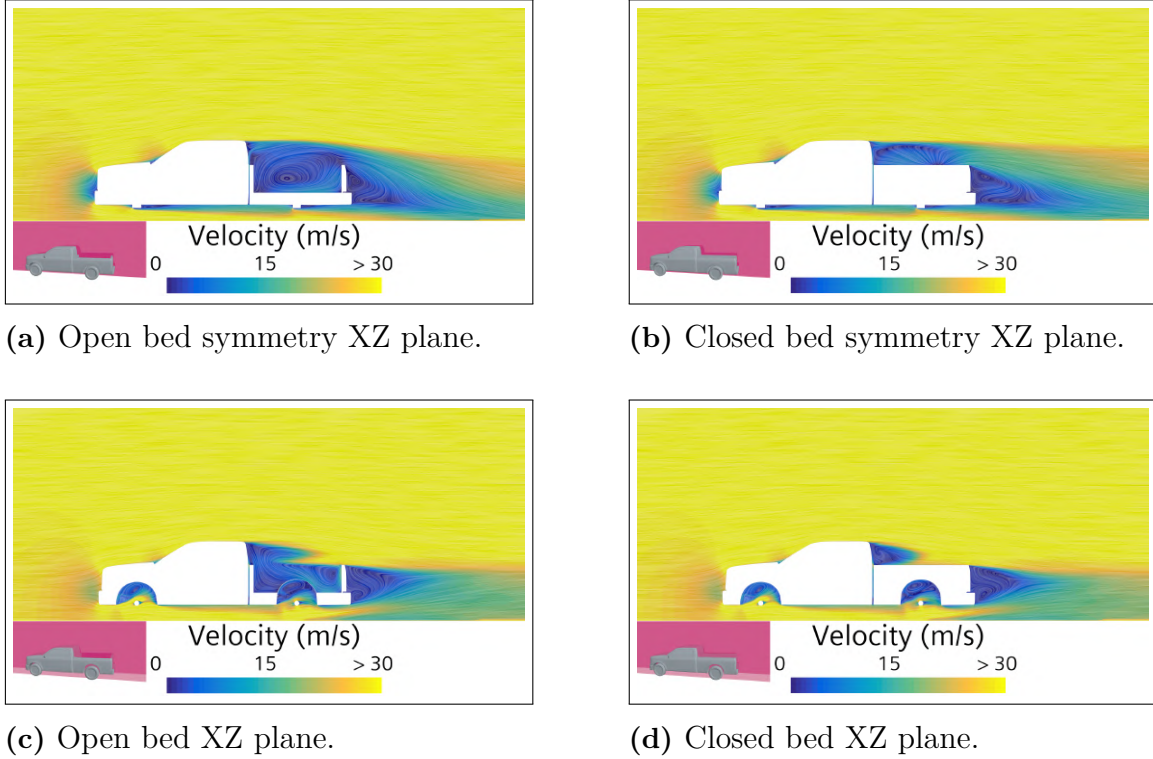


Figure 4.4: Velocity field and wake structure, closed and open bed baseline

of the RC-Vortex in the CB case, compared to the OB, and the higher coefficient C_L that develops in this region. However, the absence of bed covering results in a higher final value of C_L for the OB case. The final C_L values for both configurations are the following:

C_L Open bed	C_D Closed bed
0.106	0.075

Those C_L values bring a lift force of: $\approx 141\text{ N}$ for the OB case and $\approx 99.9\text{ N}$ for the CB case, equivalent respectively to -14.4 kg and -10.2 kg , for the simulation conditions. Although the magnitude of the total vertical force is small, relative to the weight of the vehicle (typically around two tonnes), a lift force applied to the rear part of the vehicle, changes the vehicle balance and reduces rear-axle cornering stiffness at highway speeds.

4.4 Drag reduction aero-development

In order to reduce the drag coefficient of a vehicle two main approach can be evaluated: optimizing the geometry of the actual vehicle, for example increasing or reducing inclination of the bonnet and windscreens, or adding/re-design vehicle elements, called add-on. The second path is the one chosen, for two main reasons: it is easier

4. Results

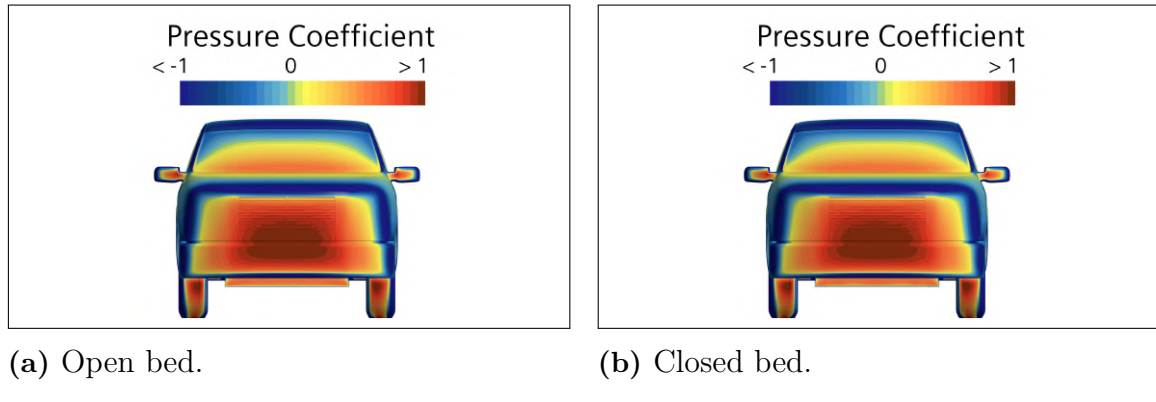


Figure 4.5: Pressure coefficient distribution on the front of the pickup baseline.

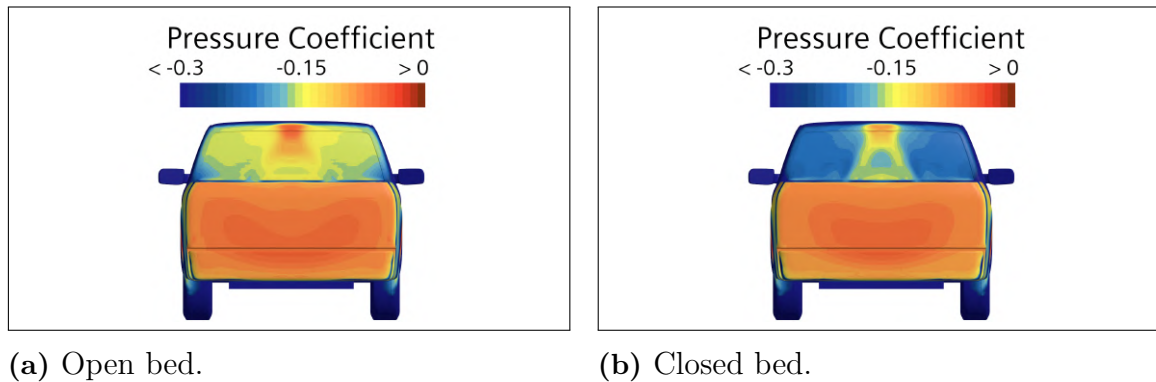


Figure 4.6: Pressure coefficient distribution on the rear of the pickup baseline.

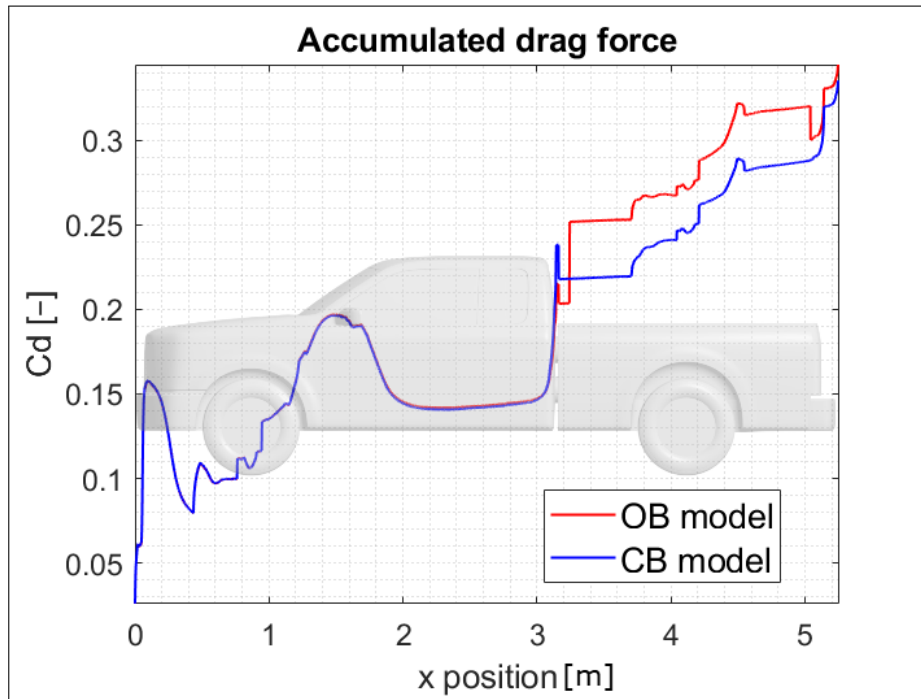
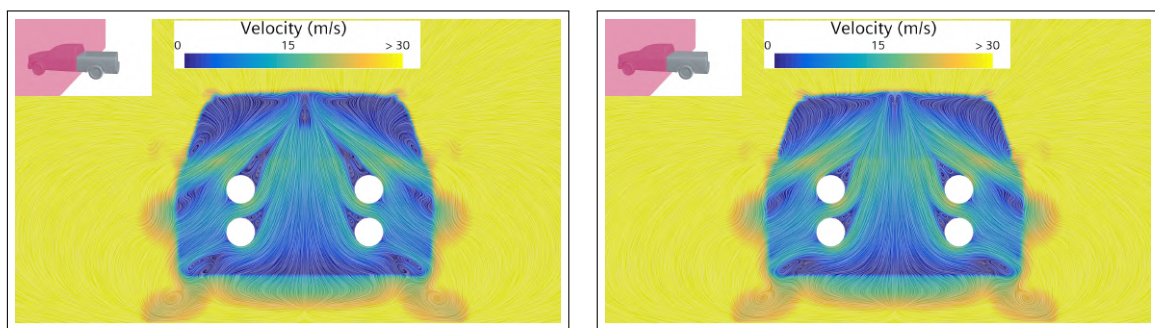


Figure 4.7: Accumulated drag coefficient open bed and closed bed baseline.

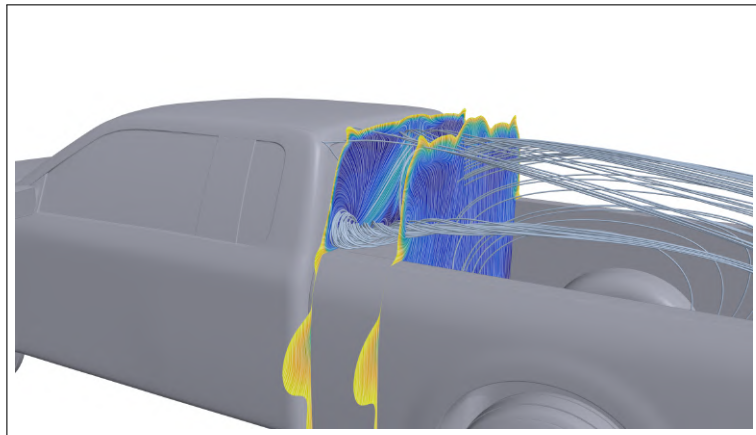


(a) Open bed baseline.

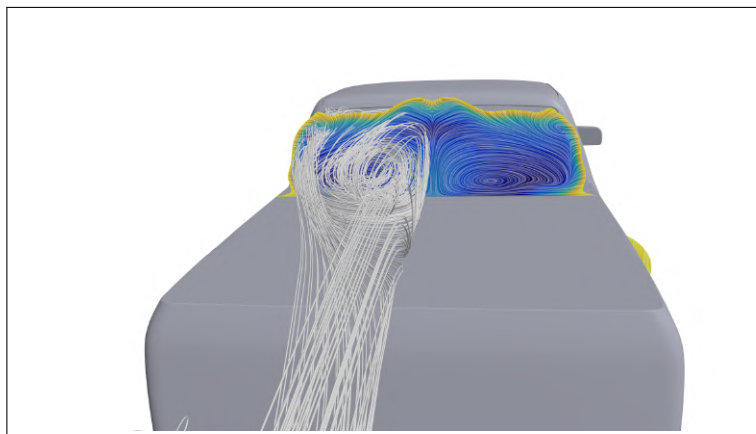
(b) Closed bed baseline.

Figure 4.8: Velocity field with convolution lines between the cabin-bed gap.

4. Results

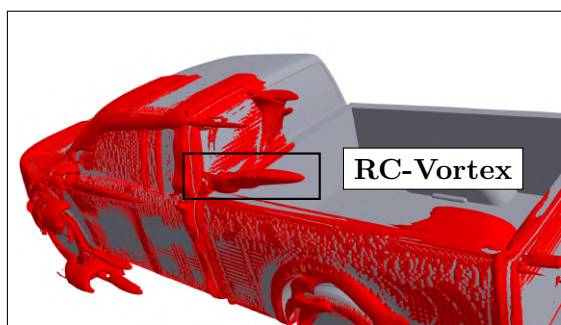


(a) Open bed.

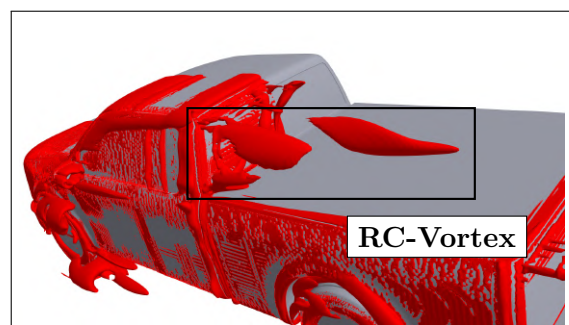


(b) Closed bed.

Figure 4.9: RC-Vortex behind the cabin, comparison open bed and closed bed baseline.

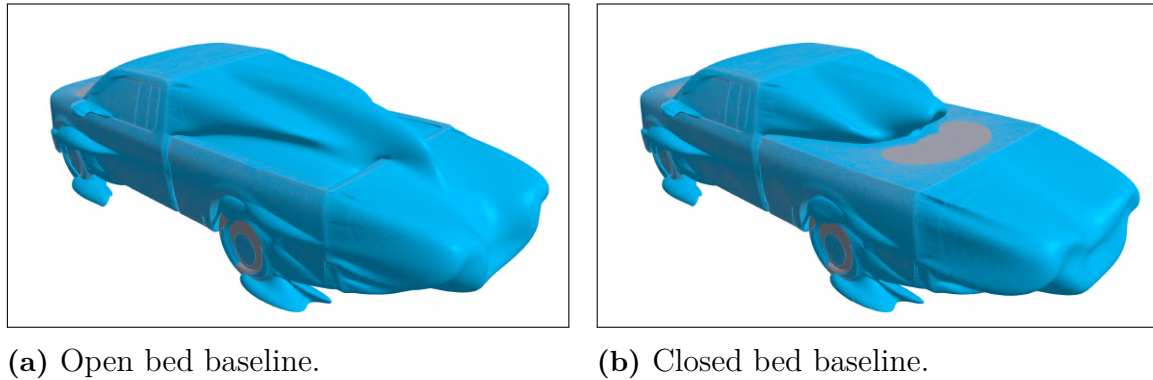


(a) Open bed baseline.



(b) Closed bed baseline.

Figure 4.10: Isosurface for Q-criterion, $Q=1500$.



(a) Open bed baseline.

(b) Closed bed baseline.

Figure 4.11: Isosurface for Total Pressure Coefficient, $C_{P_{tot}} = 0$.

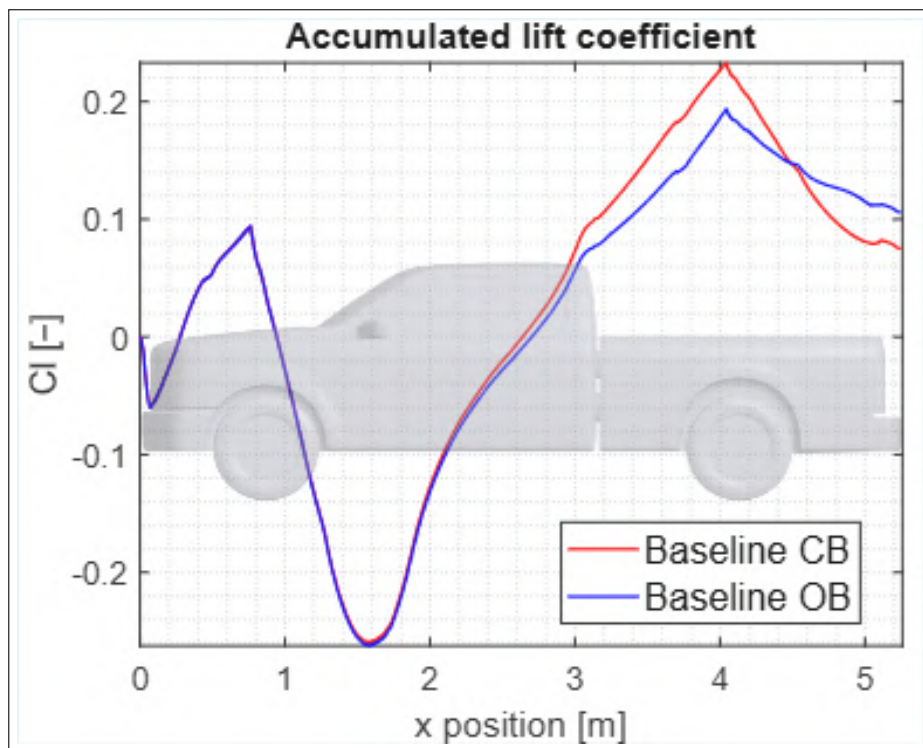


Figure 4.12: Accumulated lift coefficient open bed and closed bed baseline.

4. Results

to integrate an add-on on an already existent model without need for a complete redesign, and second the first way is much more studied and documented in literature.

An important aspect that I have tried to take into consideration is the need to develop solutions that would improve both configurations, OB and CB, or at least improve OB and be neutral for CB. I have started focusing on the rear cabin area and exploring simple design corrections. All the following modifications have been tested on the open bed pickup. Only after identifying the best solution, this was applied and verified on the closed bed case. This approach was necessary due to limited time and computational resources.

4.4.1 Closing the gap

As already discussed in Section 4.3 the presence of empty space between the passenger's cabin and the bed has a significant relevance in promoting counter rotating vortices behind the cabin itself. Of course, the first modification tested was to seal this gap. Figure 4.13 show the modified configuration with the gap closed.

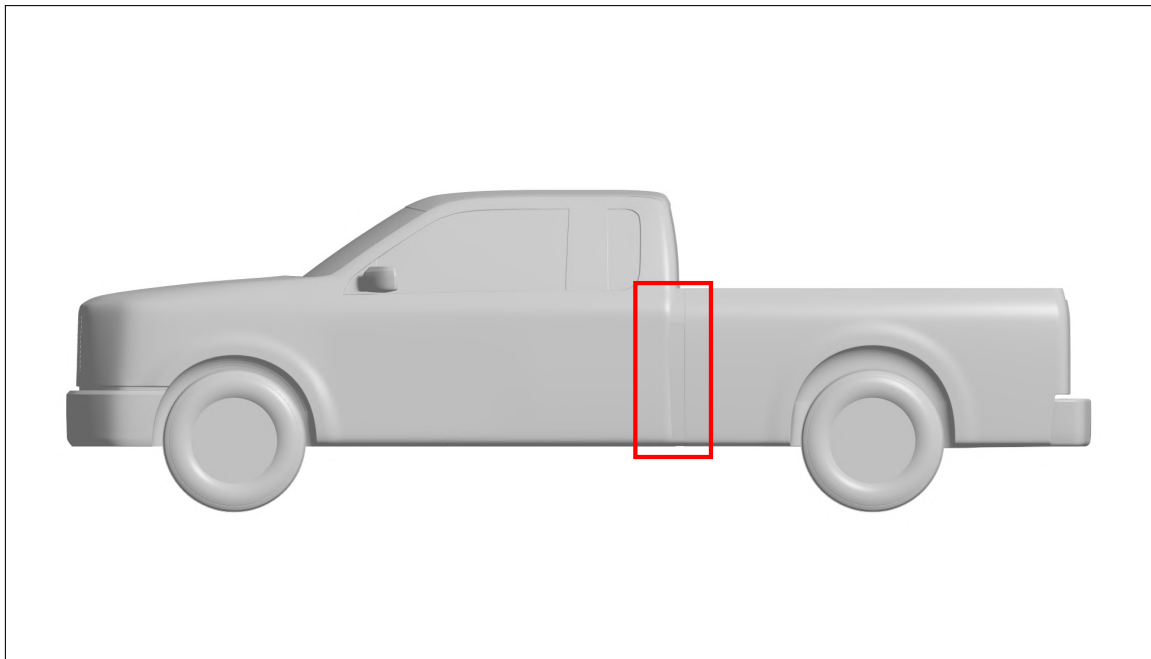
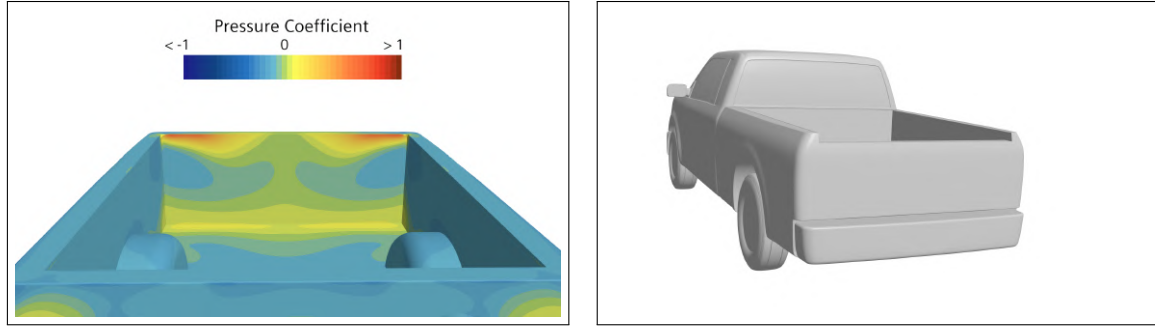


Figure 4.13: Side view of base line pickup with the cabin-bed gap closed.

4.4.2 Cutting the tailgate

Analysing the pressure distribution on the tailgate, Figure 4.14a, it is possible to notice how there is a small region of high pressure coefficient on the top edge of the

tailgate itself. The idea is to cut 6 cm of the gate starting from the top to eliminate the relative area.



(a) C_P values on tailgate. (b) Tailgate cut by 6 cm.

Figure 4.14: Tailgate modification.

4.4.3 Rear-cab spoiler

Inspired by the work of M. Urquart [30], I designed a rear spoiler for the cab with the intention of generating a cavity effect at the rear of the cab itself, with the additional aim of increasing the downwash effect to reduce the size of the wake. The spoiler consists of two vertical bulkheads and a transverse wing with a NACA0012 profile and a 10° angle of attack. Figures 4.15 and 4.16 show the design of the spoiler and Figure 4.17 report the two possible configurations in which the spoiler can be mounted on the pickup.

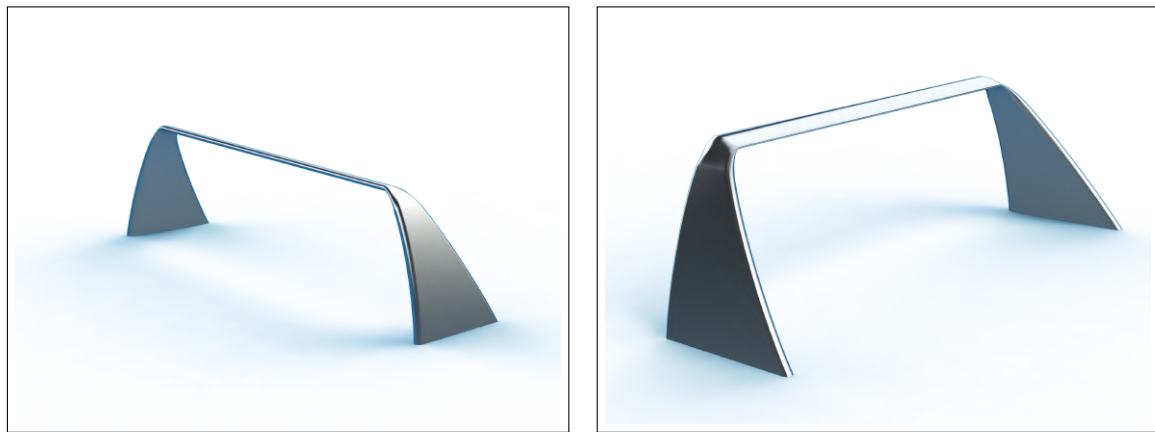


Figure 4.15: Rear-cab spoiler front and back view.

4. Results

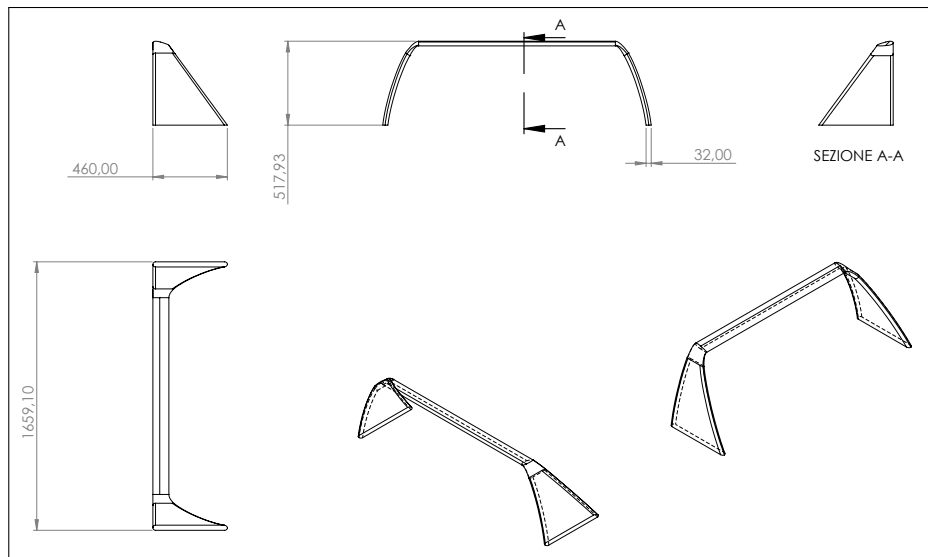
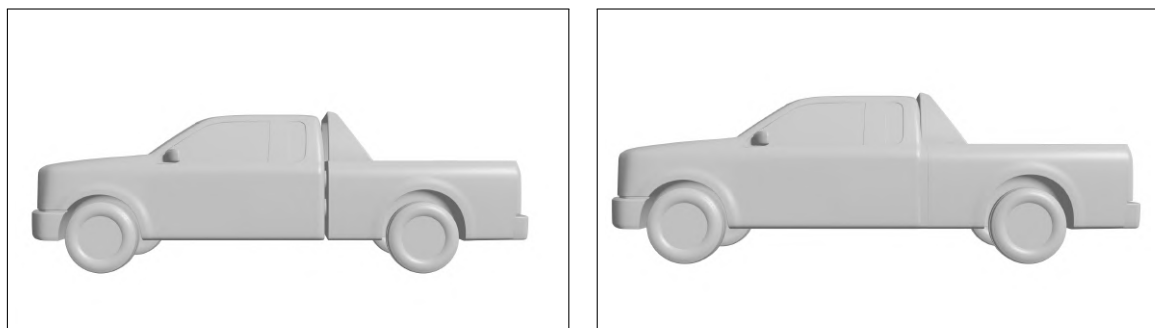


Figure 4.16: Spoiler projection draw, measures in millimetres.



(a) Spoiler separated from the cabin side view.

(b) Spoiler attached to the cabin with closed gap side view.

Figure 4.17: The two spoiler configurations.

4.4.4 Optimal configuration

The three previous design modifications presented can be tested alone or in combination. To list all configurations tested without ambiguities, a unique code is assigned to each configuration, following Table 4.3. The drag coefficient for each

Design configuration	Code
Only closed gap	Clsg
Only tailgate cut	GatC
Spoiler separated from the cabin	SplSpr
Spoiler attached to the cabin (always with the gap closed)	SplAttc
Example of combination: Spoiler separated from cabin + Tailgate cut	SplSpr-GatC

Table 4.3: Design modification configuration identification code.

configuration studied is listed in Table 4.4 with relative variation with respect to the baseline. Notice that all the configurations are applied to the open bed pickup. From table 4.4, it can be seen that cutting 6 cm off the tailgate (GatC) does not

Configuration	C_D	Δ with baseline
Clsg	0.338	-2.0%
GatC	0.345	+0.0%
GatC-Clsg	0.339	-1.7%
SplSpr	0.337	-2.3%
SplSpr-GatC	0.339	-1.7%
SplSpr-Clsg	0.337	-2.3%
SplSpr-Clsg-GatC	0.338	-2.0%
SplAttc	0.334	-3.2%
SplAttc-GatC	0.336	-2.6%

Table 4.4: Effect of the introduced modifications.

4. Results

provide any benefit and is even detrimental if the cut is made in the presence of a spoiler (SplSpr-GatC), reducing the efficiency gain compared to the case of the spoiler alone (SplSpr). On the other hand, closing the cabin-bed gap leads to a relevant gain of about -2% . This modification is relatively easy to adopt in real industrial production and it can be implemented with a simple rubber sleeve that seals the gap. The greatest reduction in drag coefficient can be achieved with the combination of the rear cabin spoiler attached to the rear cabin panel and the simultaneous closing of the gap, in Table 4.4 named SplAttc, with a gain of -3.2% .

Performing the numerical simulation for the best model with closed bed configuration the C_D obtained is 0.327, sharing a gain with respect to the baseline CB of -2.4% . In Table 4.5 are listed the drag coefficient for the best model in the OB and CB configuration and the relative gain in terms of drag coefficient.

	Best model OB	Best model CB
C_D	0.334	0.327
Δ	-3.2%	-2.4%

Table 4.5: Drag coefficient for best model OB and CB configurations, and Δ respect to relative baseline.

4.5 Best configuration analysis

The following section is completely dedicated to the comparison between the base line and the best model identified above.

Figure 4.18a and Figure 4.18b one time more underlines how acting behind the passenger cabin does not affect the front pressure distribution and local drag generation. Figure 4.18c and Figure 4.18d, on the contrary, show that closing the gap the pressure distribution on the cabin-back became more uniform. Moreover the presence of the spoiler create highly negative C_P regions on the edge of the cabin back surface and two spots of high C_P on the corner of the spoiler itself, the two small yellow spots in Figure 4.18d. This gradient in C_P distribution could lead to vortices formations and it suggest the needs for an optimization of the spoiler design and position. Further, it is relevant to notice that the average C_P on the tailgate surface is increased, giving beneficial effects on pressure drag.

The overall advantage is evident looking at Figure 4.19a. The gap closure combined with the spoiler decreases the pressure on the forward face of the tailgate and increases it on the opposite one, leading a gain of -11 drag counts.

In the case of closed bed configuration, the drag reduction in the best model configuration comes directly from less form drag generated in the cabin-bed gap region, as Figure 4.19b shows. Probably in this case, with the covered deck, it is sufficient to close the gap instead of adding the spoiler too.

Looking at Figure 4.20, it is possible to see how the design modification affects the recirculation bubble inside the bed and the wake structure, with respect to the baseline (on the left-hand side of the Figure 4.20). The downwash effect is much greater in the case of improved model, as shown in Figure 4.20b, the blue wake region is visibly smaller than in the baseline 4.20a, so the wake base area is effectively reduced. It is important to note that this downwash tendency is not as significant away from the plane of symmetry, as shown in Figure 4.20d. Furthermore, a balanced wake² is usually preferable in order to reduce drag, and the wake developed by the best model is clearly asymmetric on Z axis. These images therefore suggest once again that further optimisation of the spoiler design should be carried out and that it might also be useful to modify the rear edge of the pickup floor in order to achieve an upwash effect that seeks to increase the symmetry of the wake, without sacrificing the downwash obtained.

Figure 4.21 presents the different isosurfaces for $C_{P_{tot}} = 0$ for the open and closed bed baseline, on top, and the best model on bottom. Comparing the two open bed cases, baseline versus best model (Figures 4.21a and 4.21c). The baseline configuration exhibits a voluminous and blunt wake structure with a protrusion above the flatbed tailgate, in the central area of the pickup. In contrast, the best model presents a smoother shape. The spoiler promotes a stable recirculation bubble that acts as a fluid extension of the cabin, effectively tapering the wake and "correcting" the abrupt geometric step of the rear cabin, thereby reducing form drag. The same effect is observed in closed bed cases (Figures 4.21b and 4.21d), the advantage is not so evident, although it is slightly less effective.

Behind the cabin no more streamwise vortex is formed, Figure 4.22 shows (on the YZ plane, perpendicular to the pickup symmetry plane) the velocity and streamline projection, there is no evidence of stream-wise vortices. Figure 4.23 compares the Q-criterion, with $Q=1500$, for the baseline versus the best model. In the best models (Figures 4.23c and 4.23d) the protuberance generated by the RC-Vortex is no longer present. The same conclusions come from analysing streamlines with wide seeding points behind the cabin in the region where in the baseline there were two counter rotating vortices, Figure 4.24. Moreover, from these pictures it is evident how a bigger recirculation bubble is promoted by the presence of the spoiler.

Figure 4.25 compares the accumulated lift coefficient of the baseline with the best model, for both the OB and CB configurations. The presence of a spoiler increases

²A wake is balanced if neither downwash nor upwash dominated

4. Results

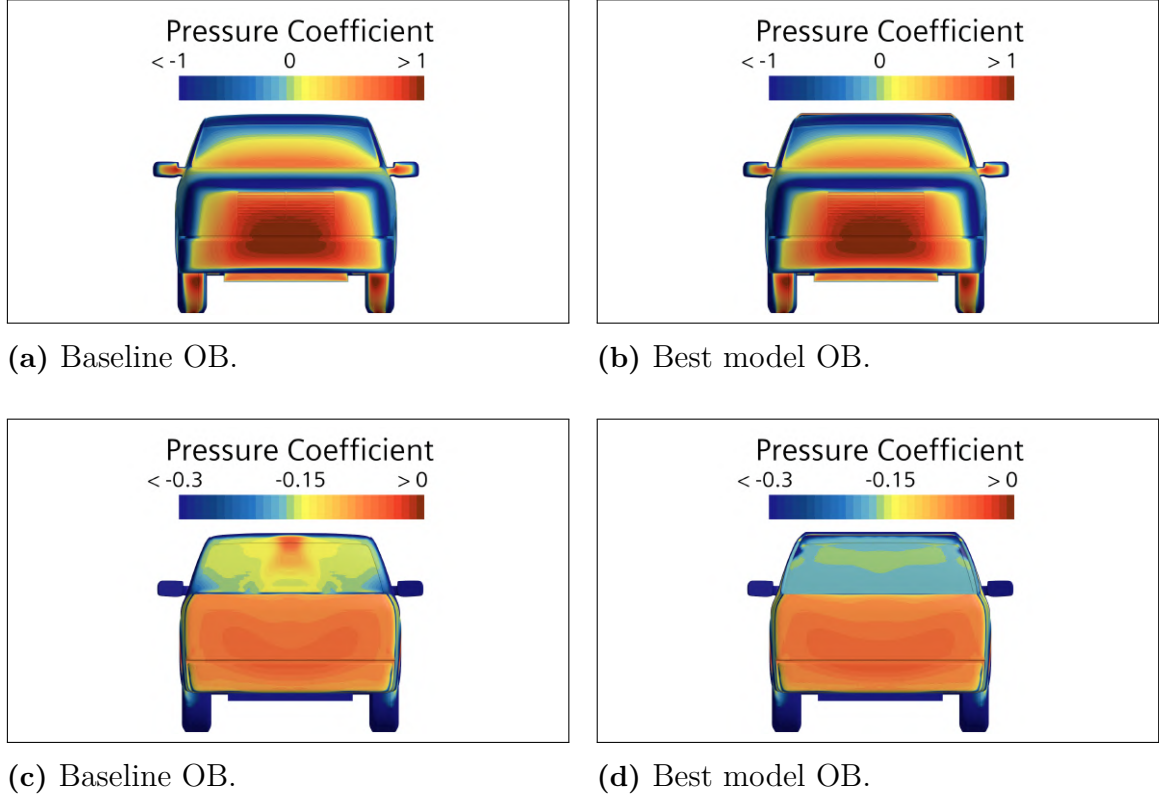


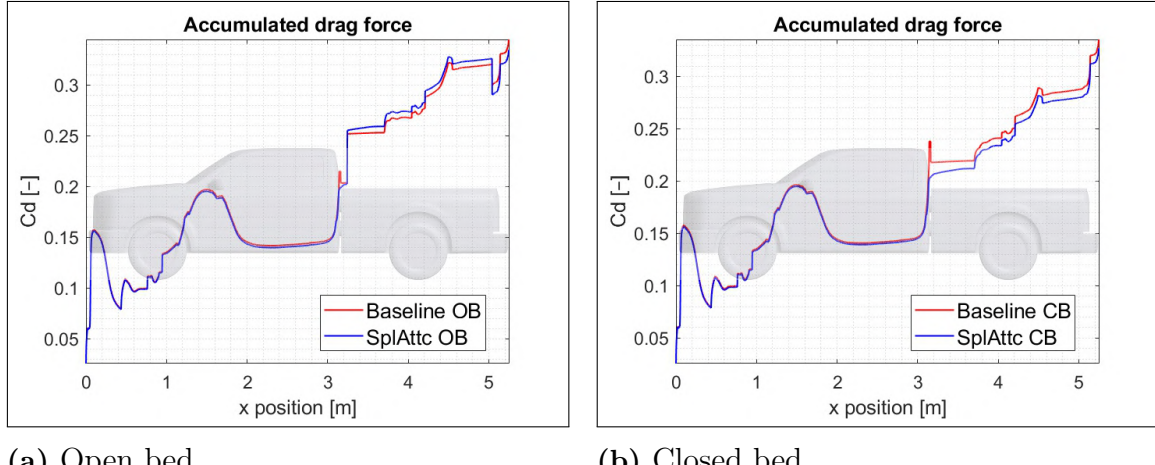
Figure 4.18: Pressure coefficient distribution on the front and rear of the pickup baseline OB and best model OB.

the lift force in both cases, but more significantly for the open bed. This result is predictable, since the spoiler has an angle of attack of 10° and increases the down-wash effect, so it generates lift by it-self. In Table 4.6 are listed the new values for C_L , the relative percentage increase with respect to the baseline, and the relative vertical force generated with simulation conditions. It is important to note that,

	Best model OB	Best model CB
C_D	0.156	0.106
Δ	+47.7%	+41.3%
Vertical force	208 N	141 N

Table 4.6: Lift coefficient for best model OB and CB configurations, Δ respect to relative baseline and relative vertical force generated with simulation conditions.

in the case of the best model, vertical force relief could become relevant for vehicle stability at very high speeds, above 120 km/h . Since a lifting force acting mainly on the rear tires of $> 30 \text{ kg}$ could generate noticeable effects, especially in wet asphalt conditions.



(a) Open bed.

(b) Closed bed.

Figure 4.19: Accumulated drag coefficient for best model both open and closed bed case.

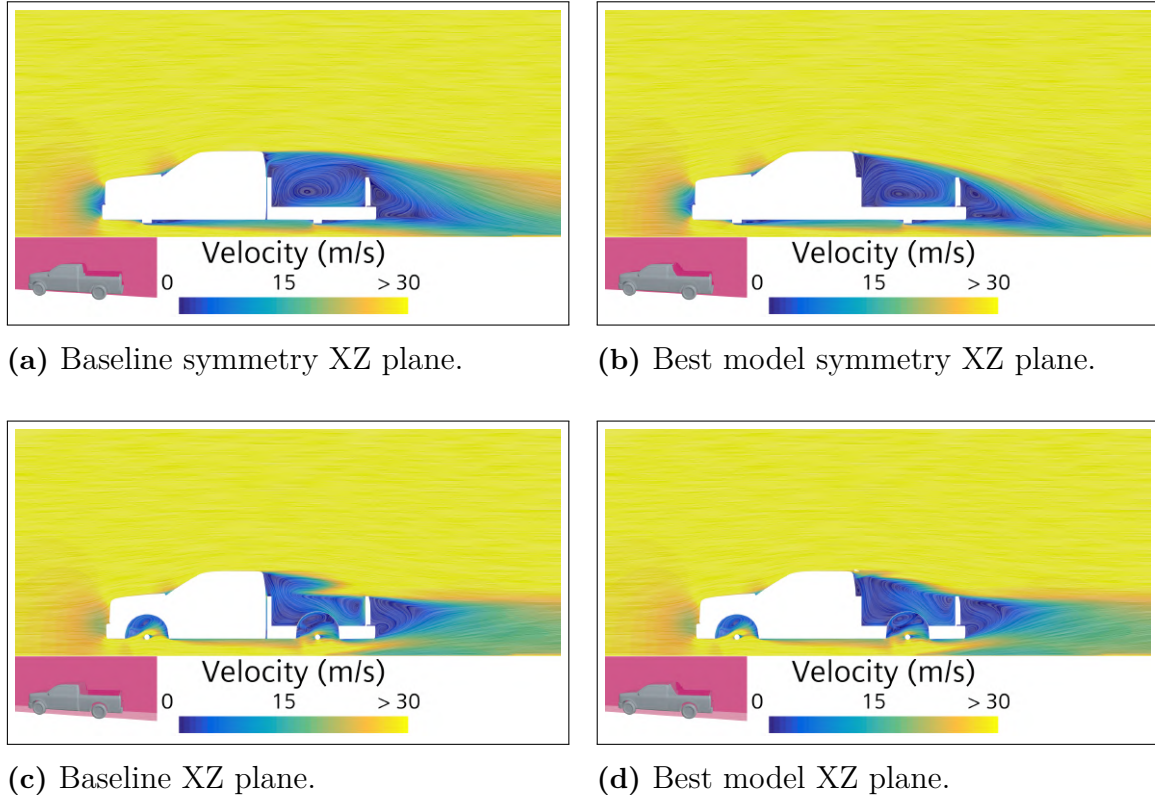


Figure 4.20: Velocity field and wake structure, open bed baseline and best model OB.

4. Results

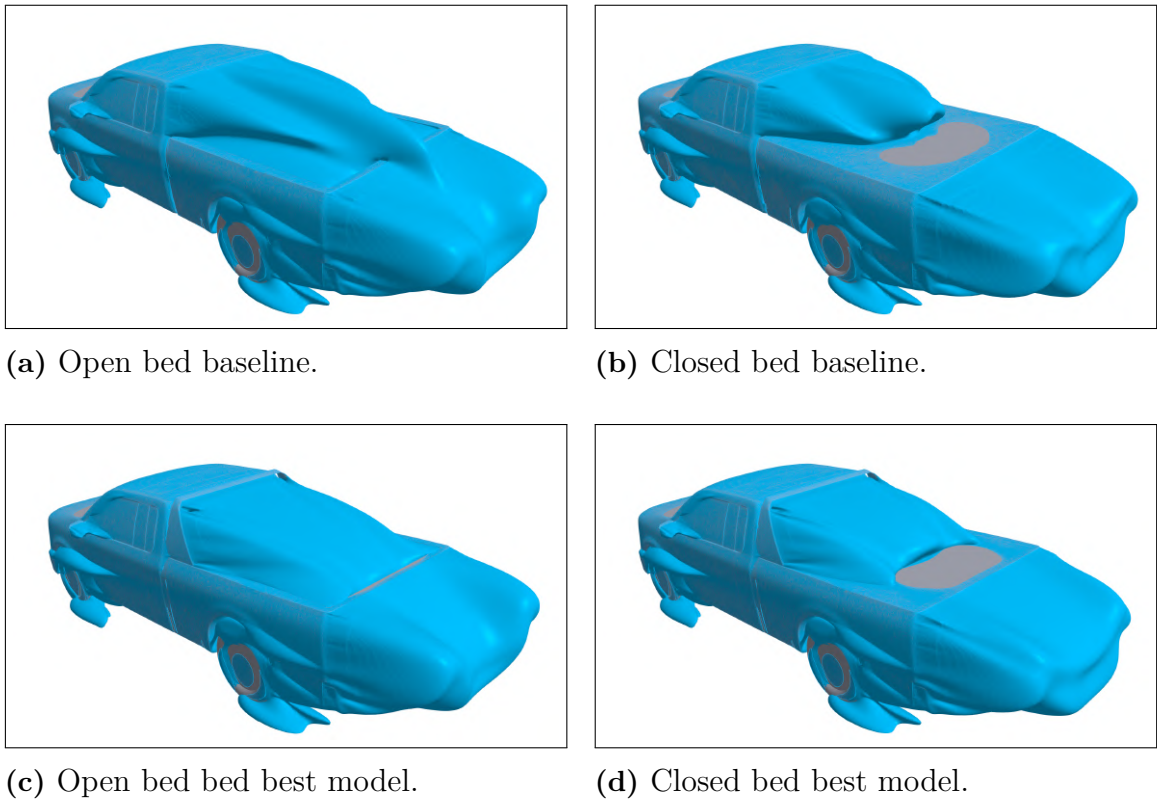


Figure 4.21: Isosurface for Total Pressure Coefficient, $C_{P_{tot}} = 0$.

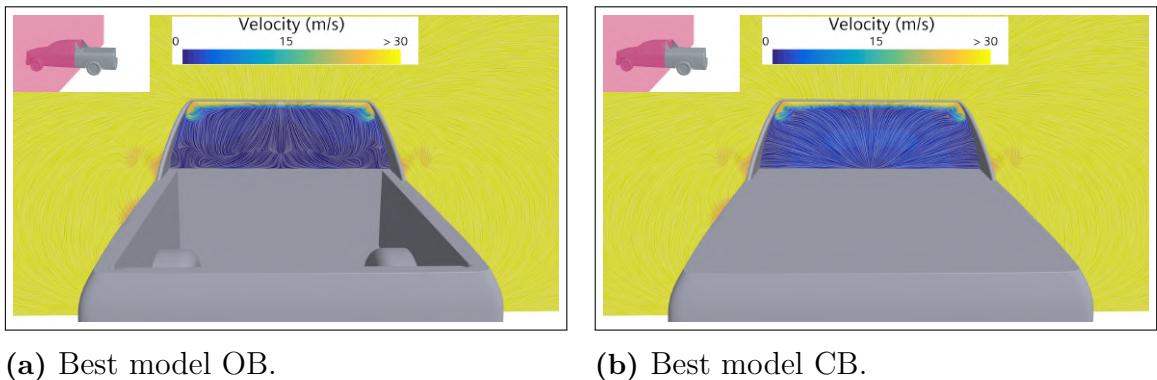


Figure 4.22: Velocity and streamline projection on YZ plane for best model.

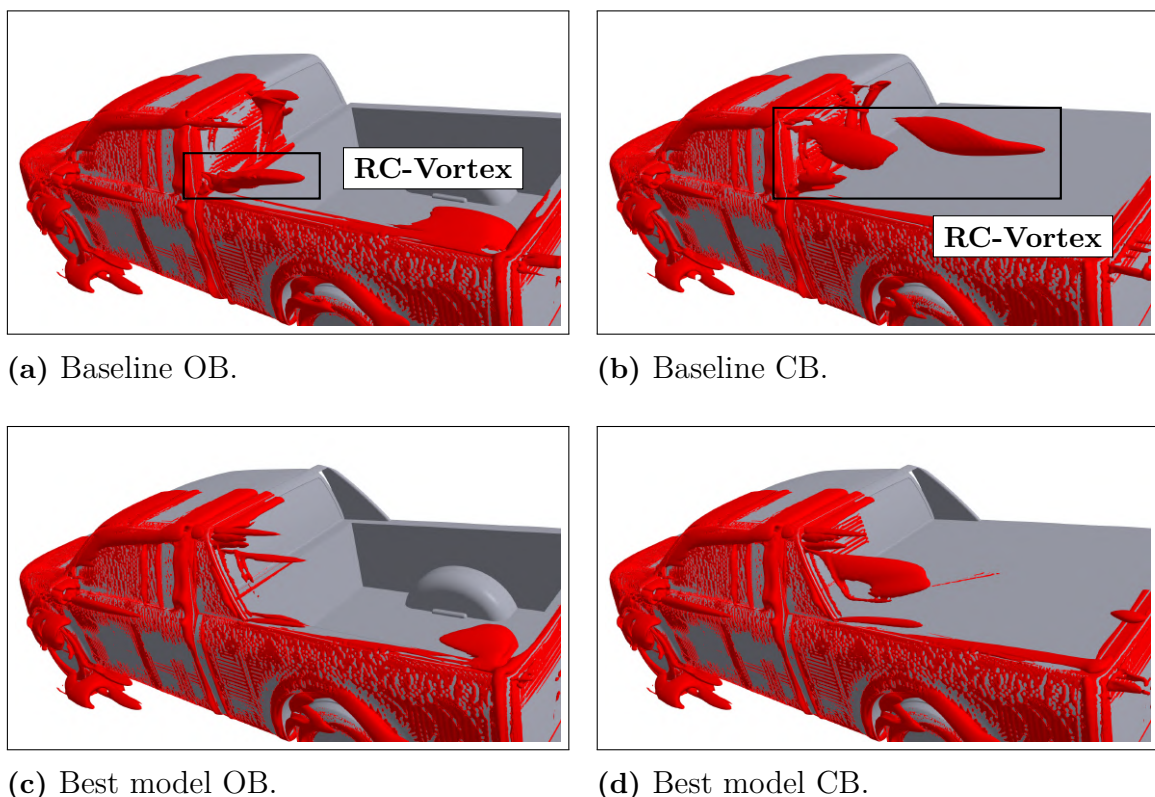
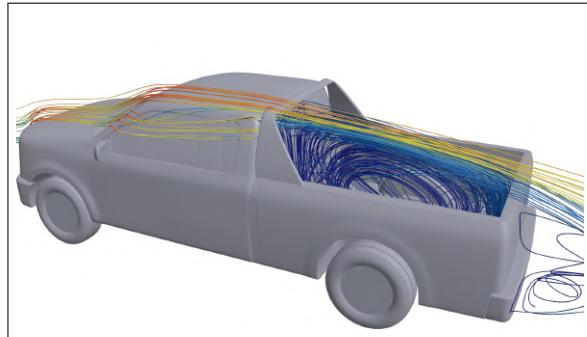
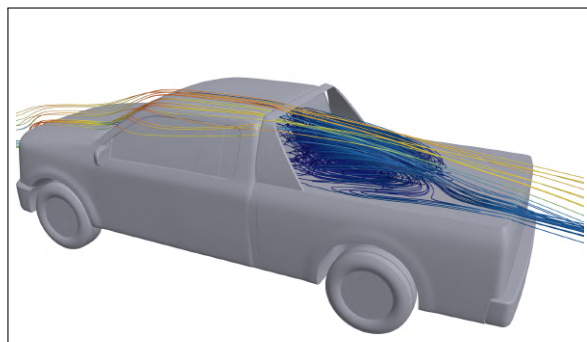


Figure 4.23: Isosurface for Q-criterion, $Q=1500$.

4. Results

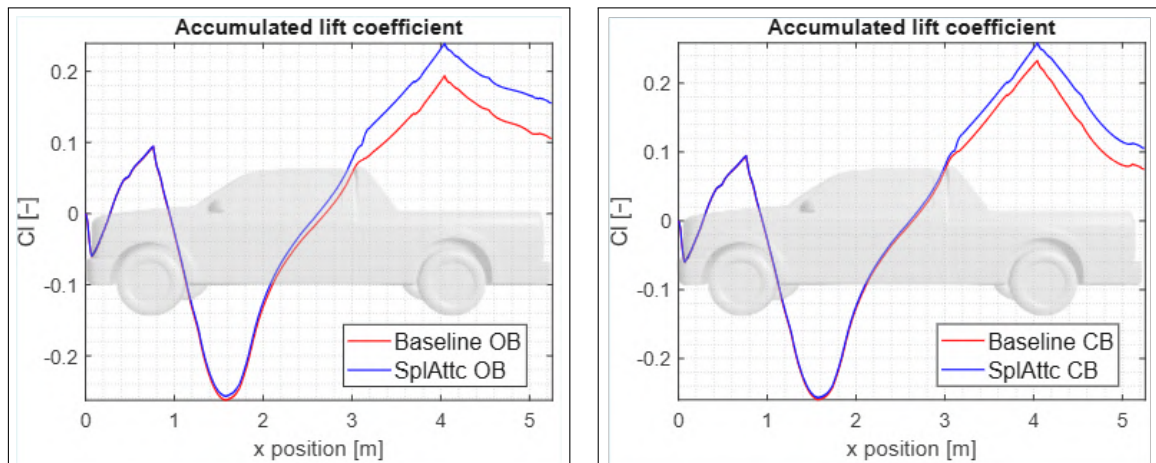


(a) Best model OB.



(b) Best model CB.

Figure 4.24: Streamlines behind the passenger cabin for best model.



(a) Open bed.

(b) Closed bed.

Figure 4.25: Accumulated lift coefficient for best model both open and closed bed case.

5

Conclusions

This thesis investigated the aerodynamics of a simplified double-cab pickup using steady RANS CFD and wind-tunnel measurements, with the goal of identifying robust, low-complexity design actions for drag reduction. Three turbulence model were assessed in Star-CCM+: Realizable $k-\varepsilon$, Lag EB $k-\varepsilon$, and SST $k-\omega$, supported by a mesh-refinement study and two near-wall strategies ($y^+ \approx 1$ and $y^+ > 30$). The adopted grid delivered consistent wall-treatment quality and asymptotic behaviour adequate for trend studies.

Wind-tunnel tests on a 1:10 model (no moving ground, no rotating wheels) provided the reference for numerical analysis validation and for evaluating wind-averaged drag. Accounting for realistic cross-wind using a standard wind-averaged formulation increased the C_D for $\beta = 0$ to $C_{D,W} = 0.381$ (OB) and 0.366 (CB), i.e., about +10%. These figures highlight the relevance of yaw in operational consumption estimates. Test-section and scaling limitations and the Reynolds number mismatch to full scale were documented and considered in the interpretation.

The Model-form comparison focused on *deltas* rather than absolute values. Using the difference $\Delta C_D = C_{D_{\text{open bed}}} - C_{D_{\text{closed bed}}}$ to reduce systematic bias, Lag EB $k\varepsilon$ proved most reliable for predicting trends across configurations, and it was used for all detailed analyses that followed.

The baseline flow topology confirmed canonical pickup features: large recirculation in the bed, a wake with downwash, and a pair of streamwise vortices shed from the cabin–bed region. The cabin–bed *gap* was identified as a key driver of adverse pressure on the rear-of-cab surface and of the bi-vortex system; OB/CB differences in this area correlated with the measured drag offset. Iso-surfaces of Q-criterion and of $C_{P_{tot}} = 0$ consistently marked loss regions and supported the diagnosis.

Three simple rear-zone edits were then screened on OB and verified on CB:

- sealing the cabin–bed gap,
- cutting 6 cm from the tailgate top edge,
- adding a rear-cab spoiler with side plates in two possible configurations, attached to or separate from the passenger cabin.

The tailgate cut gave no benefit and was detrimental with the spoiler. Gap sealing

5. Conclusions

alone reduced C_D by about -2% . The best result combined gap sealing with the attached spoiler (“SplAttc”), giving -3.2% on OB. When applied to CB, the best model yielded $C_D = 0.327$ with -2.4% respect to CB baseline.

Flow-field visualizations of the best model confirmed the mechanism: the rear-cab treatment weakens or suppresses the streamwise vortex pair, modifies the cabin-wake shear layer, and reduces the volume of the $C_{P_{tot}} = 0$ loss region in OB, consistent with the drag reduction observed. In CB, sealing the gap appears to be the primary lever; the spoiler is of secondary value when the bed is covered.

Further study possibilities are emerged during the analysis:

- targeting the underbody flow and modifying the rear diffuser geometry, could effectively balance the strong downwash generated by the cab spoiler, potentially restoring wake symmetry and further reducing drag;
- given the significant discrepancy between zero-yaw C_D and the wind averaged drag coefficient, C_{DW} , future computational campaigns should be carried out with non-zero yaw angle to numerically estimate C_{DW} and compare the value with that obtained in the wind tunnel.
- the obtained results should be verified and validated with more advanced CFD analysis, using DDES model. This approach allows for more detailed analysis and more reliable results on separation points and vortex generation.

Bibliography

- [1] J. Howell, M. Passmore, and S. Windsor, “A drag coefficient for test cycle application,” *SAE International Journal of Passenger Cars - Mechanical Systems*, vol. 11, no. 5, pp. 447–461, apr 2018. [Online]. Available: <https://doi.org/10.4271/2018-01-0742>
- [2] European Parliament, “Co2 emissions from cars: facts and figures (infographics),” <https://www.europarl.europa.eu/topics/en/article/20190313STO31218/co2-emissions-from-cars-facts-and-figures-infographics#:~:text=Passenger%20cars%20are%20a%20major,could%20help%20to%20reduce%20emissions.>, last updated: 06-12-2024.
- [3] European Envirormant Agency, “Co2 emissions performance of new passenger cars in europe,” <https://www.eea.europa.eu/en/analysis/indicators/co2-performance-of-new-passenger>, published 16 Dec 2024.
- [4] R. Barnard, *Road Vehicle Aerodynamic Design: An Introduction*, 3rd ed. MechAero Publishing, 2009.
- [5] W. H. Hucho, Ed., *Aerodynamics of Road Vehicles: From Fluid Mechanics to Vehicle Engineering*, 5th ed. Warrendale, PA: SAE International, 2013, cited as Chapter 7.
- [6] K. Min Seok, B. Yein, K. Jongwon, K. Jongwon, and K. Taek Keun, “Optimal Design of an Ecofriendly Pickup Truck Overhang and Roof to Reduce the Drag Coefficient,” *arXiv:1907.09415v5 [quant-ph]*, 5 2024.
- [7] S. Holloway, J. Leylek, W. York, and B. Khalighi, “Aerodynamics of a pickup truck: Combined cfd and experimental study,” *SAE International Journal of Commercial Vehicles*, vol. 2, pp. 88–100, 10 2009.
- [8] J. Howell and A. Gaylard, “Improving suv aerodynamics,” 10 2006.
- [9] Wikipedia, “Worldwide harmonised light vehicles test procedure,” https://en.wikipedia.org/wiki/Worldwide_Harmonised_Light_Vehicles_Test_Procedure#WLTC_driving_cycles.
- [10] Wikipedia, “Range anxiety,” https://en.wikipedia.org/wiki/Range_anxiety.
- [11] Straits Research, “Pickup trucks market size, share & trends analysis report by vehicle type, by fuel type, by drivetrain and by region forecasts, 2025-2033,” https://straitsresearch.com/report/pickup-trucks-market?utm_source=chatgpt.com.

Bibliography

- [12] Scopus, <https://www.scopus.com/search/form.uri?display=basic&zone=header&origin=#basic>.
- [13] K. R. Cooper, “Pickup truck aerodynamics – keep your tailgate up,” SAE International, Tech. Rep. 2004-01-1146, 2004.
- [14] M. Urquhart, “Vehicle wakes in side wind,” PhD Thesis, Chalmers University of Technology, 2021.
- [15] M. Lehmann, <https://github.com/ProjectPhysX/FluidX3D>.
- [16] Siemens Digital Industries Software, *STAR-CCM+ User Guide*, 2024.
- [17] V. Giovacchini, “Development of a numerical platform for the modeling and optimal control of liquid metal flows,” Ph.D. dissertation, alma, Luglio 2022. [Online]. Available: <https://amsdottorato.unibo.it/id/eprint/10269/>
- [18] B. Launder and D. Spalding, “The numerical computation of turbulent flows,” *Computer Methods in Applied Mechanics and Engineering*, vol. 3, no. 2, pp. 269–289, 1974. [Online]. Available: <https://www.sciencedirect.com/science/article/pii/0045782574900292>
- [19] T. H. Shih, W. W. Liou, A. Shabbir, Z. Yang, and J. Zhu, “A new $k-\varepsilon$ eddy viscosity model for high reynolds number turbulent flows,” *Computers & Fluids*, vol. 24, no. 3, pp. 227–238, 1995. [Online]. Available: <https://www.sciencedirect.com/science/article/pii/004579309400032T>
- [20] P. Spalart and S. Almaras, “A one-equation turbulence model for aerodynamic flows,” 1994. [Online]. Available: <https://arc.aiaa.org/doi/abs/10.2514/6.1992-439>
- [21] S. Lardeau and F. Billard, “Development of an elliptic-blending lag model for industrial applications,” 2016. [Online]. Available: <https://arc.aiaa.org/doi/abs/10.2514/6.2016-1600>
- [22] R. Manceau and K. Hanjalić, “Elliptic blending model: A new near-wall reynolds-stress turbulence closure,” *Physics of Fluids*, vol. 14, no. 2, pp. 744–754, 02 2002. [Online]. Available: <https://doi.org/10.1063/1.1432693>
- [23] A. Revell, S. Benhamadouche, T. Craft, and D. Laurence, “A stress-strain lag eddy viscosity model for unsteady mean flow,” *International Journal of Heat and Fluid Flow*, vol. 27, no. 5, pp. 821–830, 2006, special issue of the 6th International Symposium on Engineering Turbulence Modelling and Measurements – ETMM6. [Online]. Available: <https://www.sciencedirect.com/science/article/pii/S0142727X06000774>
- [24] F. R. Menter, “Two-equation eddy-viscosity turbulence models for engineering applications,” *AIAA Journal*, vol. 32, no. 8, pp. 1598–1605, 1994. [Online]. Available: <https://doi.org/10.2514/3.12149>
- [25] S. Woodiga, P. Norman, K. Howard, N. Lewington, R. Carstairs, B. Hupertz, and K. Chalupa, “The gtu - a new realistic generic pickup truck and suv model,” 04 2020.
- [26] W. Meile, T. Ladinek, G. Brenn, A. Reppenhagen, and A. Fuchs, “Non-symmetric bi-stable flow around the ahmed body,” *International Journal*

of Heat and Fluid Flow, vol. 57, pp. 34–47, 2016. [Online]. Available: <https://www.sciencedirect.com/science/article/pii/S0142727X15001320>

[27] M. Grandemange, M. Gohlke, and O. Cadot, “Turbulent wake past a three-dimensional blunt body. part 1. global modes and bi-stability,” *Journal of Fluid Mechanics*, vol. 722, p. 51–84, 2013.

[28] P. J. Roache, “Perspective: A method for uniform reporting of grid refinement studies,” *Journal of Fluids Engineering; (United States)*, vol. 116:3, 09 1994. [Online]. Available: <https://www.osti.gov/biblio/6817347>

[29] J. Jeong and F. Hussain, “On the identification of a vortex,” *Journal of Fluid Mechanics*, vol. 285, p. 69–94, 1995.

[30] M. Urquhart, S. Sebben, and L. Sterken, “Numerical analysis of a vehicle wake with tapered rear extensions under yaw conditions,” *Journal of Wind Engineering and Industrial Aerodynamics*, vol. 179, pp. 308–318, 2018. [Online]. Available: <https://www.sciencedirect.com/science/article/pii/S0167610518301144>

Bibliography

DEPARTMENT OF INDUSTRIAL ENGINEERING
UNIVERSITÀ DI BOLOGNA
Forlì, Italy



ALMA MATER STUDIORUM
UNIVERSITÀ DI BOLOGNA